



$^{40}\text{Ar} / ^{39}\text{Ar}$ age constraints on the formation of fluid-rich quartz veins from the NW Rhenohercynian zone (Rursee area, Germany)

Akbar Aydin Oglu Huseynov, Jan Wijbrans, Klaudia Kuiper, and Jeroen van der Lubbe

Department of Earth Sciences, Vrije Universiteit Amsterdam, De Boelelaan 1085, 1081 HV Amsterdam, the Netherlands

Correspondence: Akbar Aydin Oglu Huseynov (a.huseynov@vu.nl)

Received: 11 December 2024 – Discussion started: 9 January 2025

Revised: 10 March 2025 – Accepted: 11 March 2025 – Published: 15 May 2025

Abstract. A substantial part of the subsurface geology in northwestern and central Europe is defined by the late Palaeozoic Variscan Orogeny (~ 350 Ma). Our focus is mainly on veining in anchimetamorphic sedimentary rocks affected by this orogeny. Mineral veins serve as repositories for documenting the origin of subsurface fluid flows and dynamics, and dating them may provide crucial insight into the timing of orogenic and possible reactivation events. The Rursee area (Rhenish Massif, Germany), part of the Variscan foreland zone on the Avalonia microcontinent, represents a key locality for studying Variscan quartz vein formation. Based on structural grounds, two groups/types of Rursee quartz veins have been linked with the early stages of Variscan, but their absolute ages are still unknown.

The aim of this study is to date these quartz veins using the $^{40}\text{Ar} / ^{39}\text{Ar}$ stepwise crushing method based on the radioactive decay of ^{40}K dissolved in high-salinity fluid inclusions. We obtained Jurassic to Cretaceous ages, and isotopic analysis of the argon gases revealed that the fluid-rich quartz fractions release ^{39}Ar in two distinct phases. Regardless of the salinity of fluid inclusions in quartz veins, stepwise crushing provides apparent $\text{K} / \text{Cl} > 1$. Electron probe micro-analyser data confirm the presence of K (^{39}Ar) in the K-bearing mineral inclusions (e.g. sericite, white mica, and chlorite) and microcracks and possibly in the crystal lattice of quartz.

Secondary fluid inclusions or K-bearing mineral inclusions and/or the crystal lattice of quartz, which formed subsequently in the Variscan vein fractures, provide a plausible explanation for the young apparent isotopic ages. Deformation-induced quartz sub-grains may suggest that obtained maximum apparent ages are likely to reflect post-Variscan fluid-

assisted reactivation–recrystallization due to tectonic activity or its cooling moment during the Jurassic–Cretaceous period rather than the original Variscan vein formation.

1 Introduction

Quartz veins are abundant in metamorphosed terranes and sedimentary basins filled with siliciclastic sediments, witnessing significant fluid movement during diagenesis and metamorphism (Yardley, 1983; Mullis et al., 1994; Cartwright and Buick, 2000; Oliver and Bons, 2001). An increase in both temperature and pressure during burial diagenesis, orogenesis, and deformation causes sedimentary and volcanic rocks to lose their volatile components and to release warm fluids, which cumulate minerals in fractures and faults (Baumgartner and Ferry, 1991; Yardley and Bottrell, 1993; Oliver and Bons, 2001; Cox, 2007). These often saline fluids contain, among others, $\text{KCl}_{(\text{aq})}$ or $\text{K}_2\text{CO}_3_{(\text{aq})}$ (Rauchenstein-Martinek et al., 2014), which are partly precipitated during the crystallization of minerals in veins or as inclusions in these minerals (Sterner et al., 1988). One of the isotopes of potassium, ^{40}K , is radioactive and can be used for K–Ar or its derivative, $^{40}\text{Ar} / ^{39}\text{Ar}$ dating. Progressive crushing techniques enable the liberation of gases from fluid inclusions, mineral inclusions, and/or crystal lattice for the age determination of geological events provided that K concentrations are high enough (Qiu and Dai, 1989; Turner and Bannon, 1992; Turner and Wang, 1992; Qiu, 1996; Kendrick et al., 2001; Qiu and Wijbrans, 2006; Kendrick et al., 2006; Qiu and Wijbrans, 2008; Qiu and Jiang, 2007; Jiang et al.,

2012; Bai et al., 2013; Liu et al., 2015). This method not only defines an age but also quantifies the ratio of noble gases (e.g. $^{39}\text{Ar}_\text{K}/^{37}\text{Ar}_\text{Ca}$, $^{39}\text{Ar}_\text{K}/^{38}\text{Ar}_\text{Cl}$) derived from Ca, K, and Cl, respectively, that have been formed during neutron radiation before analysis. The $^{39}\text{Ar}_\text{K}/^{38}\text{Ar}_\text{Cl}$ provides crucial information on the composition of parental fluids and their sources (Sumino et al., 2011; Cartwright et al., 2013). Beyond studies on fluid composition and provenance (Kelley et al., 1986; Turner and Bannon, 1992; Kendrick et al., 2001, 2006), the initial $^{40}\text{Ar}/^{36}\text{Ar}$ values of fluid inclusions in quartz can considerably vary and may be used to differentiate between meteoric-sourced water (~ 298.6) (Ballentine et al., 2002; Ozima and Podosek, 2002) and deeper crustal or mantle-derived fluids ($> 10\,000$; MORB $> 40\,000$) (Burnard et al., 1997). Additionally, hydrothermal waters can present sub-atmospheric $^{40}\text{Ar}/^{39}\text{Ar}$ ratios, as can be deduced from inverse isochrons of fluid-altered rocks (e.g. 280–290; Baksi, 2007).

To accurately determine the age of fluid inclusions in quartz veins using the $^{40}\text{Ar}/^{39}\text{Ar}$ stepwise crushing method or the source of the fluid based on $^{40}\text{Ar}/^{36}\text{Ar}$ ratios, it is necessary to consider three distinct components of ^{40}Ar , namely (1) radiogenic $^{40}\text{Ar}_\text{R}$ or $^{40}\text{Ar}^*$, which is produced in the sample itself through the radioactive decay of ^{40}K , and (2) ^{40}Ar that was initially trapped in the fluid inclusion, either as (2a) atmospheric $^{40}\text{Ar}_\text{A}$ or (2b) excess $^{40}\text{Ar}_\text{E}$. The presence of $^{40}\text{Ar}_\text{E}$ in fluid inclusions could be a challenge in determining accurate vein formation ages using the K–Ar dating technique (Rama et al., 1965). More recently, isochron diagrams using $^{40}\text{Ar}/^{39}\text{Ar}$ geochronology helped to overcome this issue (McKee et al., 1993; Qiu, 1996; Qiu et al., 2002). In addition to $^{40}\text{Ar}_\text{E}$, the origin of $^{39}\text{Ar}_\text{K}$ (or K content) has been a topic of debate, with the possibility that the $^{39}\text{Ar}_\text{K}$ (and thus K) may come from the dissolved salts in fluid inclusions, leaking from the crystal lattice during crushing (Kendrick et al., 2011), and/or from any K-bearing mineral inclusions trapped inside the crystals (Qiu and Wijbrans, 2006; Kendrick, 2007; Qiu and Wijbrans, 2009; Kendrick and Phillips, 2009).

This study aims (i) to determine the absolute age of quartz vein formation by analysing fluid inclusions using the stepwise crushing $^{40}\text{Ar}/^{39}\text{Ar}$ dating method, (ii) to elucidate the location of K in the vein minerals (e.g. fluid inclusions, mineral inclusions, and/or crystal lattice), and (iii) to identify when different K sources release their $^{39}\text{Ar}_\text{K}$ through the examination of released argon gases during the crushing process and geochemical analysis of quartz mineral samples using an electron probe micro-analyser (EPMA).

Quartz samples were obtained from an outcrop near the Rursee in the upper reaches of the Rur River in the North Eifel region of western Germany. Detailed structural investigations of this area have been previously conducted by Van Noten et al. (2007), who differentiated quartz veins into two groups. The older generation of quartz veins, the so-called bedding-normal veins (BNVs), is assigned to the early stages

of the Variscan Orogeny, and the second group, comprising bedding-parallel veins (BPVs), is linked to the main stage of the Variscan Orogeny. Absolute $^{40}\text{Ar}/^{39}\text{Ar}$ ages of fluid inclusions representing the age of quartz vein formation would allow us to better constrain the structural evolution and sub-surface fluid flow during the Variscan Orogeny in northwestern Europe. Reliable $^{40}\text{Ar}/^{39}\text{Ar}$ age constraints of quartz vein formation would provide the opportunity to understand the timing and evolution of mountain building in analogue fold-and-thrust belts.

Geological setting

The Rhenohercynian fold-and-thrust belt, part of the Variscan, is primarily located in the Rhenish Massif in Germany and extends westward into the Ardennes, southwest England, and eastward to the Harz Mountains (Kötonik et al., 2018). The Ardennes allochthon (Fig. 1a), the western part of the Rhenish Massif, structurally comprises three main components: the Dinant fold-and-thrust belt, the lower Palaeozoic inliers, and the High-Ardenne Slate Belt (HASB). The HASB primarily consists of Lower Devonian metasediments, including the Rurberg (upper Pragian) and Heimbach (upper Pragian to lower Emsian) units.

For this study, quartz vein samples were collected near the Schwammenauel dam in the Rursee area of the North Eifel region, Germany (Fig. 1b). The Rurberg and Heimbach units feature alternating layers of siltstones and fine- to coarse-grained sandstones (Goemaere and Dejonghe, 2005), deposited in shallow marine to deltaic environments in the northern Rhenohercynian Ocean (Oncken et al., 1999). The Early Devonian strata have accumulated to a total thickness of up to 7 km due to rapid subsidence and deposition (von Winterfeld, 1994), forming the Eifel syncline (Fig. 1b). These strata are overlain by a ~ 3 km thick sequence of lower Lochkovian to Pragian deposits.

The late Carboniferous deformation of the Variscan foreland led to initial burial metamorphism (Mansy et al., 1999), with prehnite–pumpellyite facies similar to the anchizone conditions in the North Eifel area (Fielitz, 1995), where temperatures reached up to 220 °C (Littke et al., 2012). There is also evidence of the upward migration of warm fluids into the northern Variscan front in the Ardennes, driven by Variscan thrusting (Mucchez et al., 2000; Schroyen and Mucchez, 2000; Lünenschloss et al., 2008).

Following the Variscan period, the Rhenish Massif has been affected by transpressional and transtensional deformation that resulted in the formation of complex fault networks that host vein mineralization (Franzke and Anderle, 1995; Ziegler and Dèzes, 2005). During the Jurassic–Cretaceous period, the southern Rhenish Massif was periodically affected by hydrothermal activities (Kirnbauer et al., 2012), as indicated by geochronological data for post-Variscan vein mineralization (Bonhomme et al., 1983; Mertz et al., 1986; Bähr, 1987; Jakobus, 1992; Hein and Behr, 1994; Klügel,

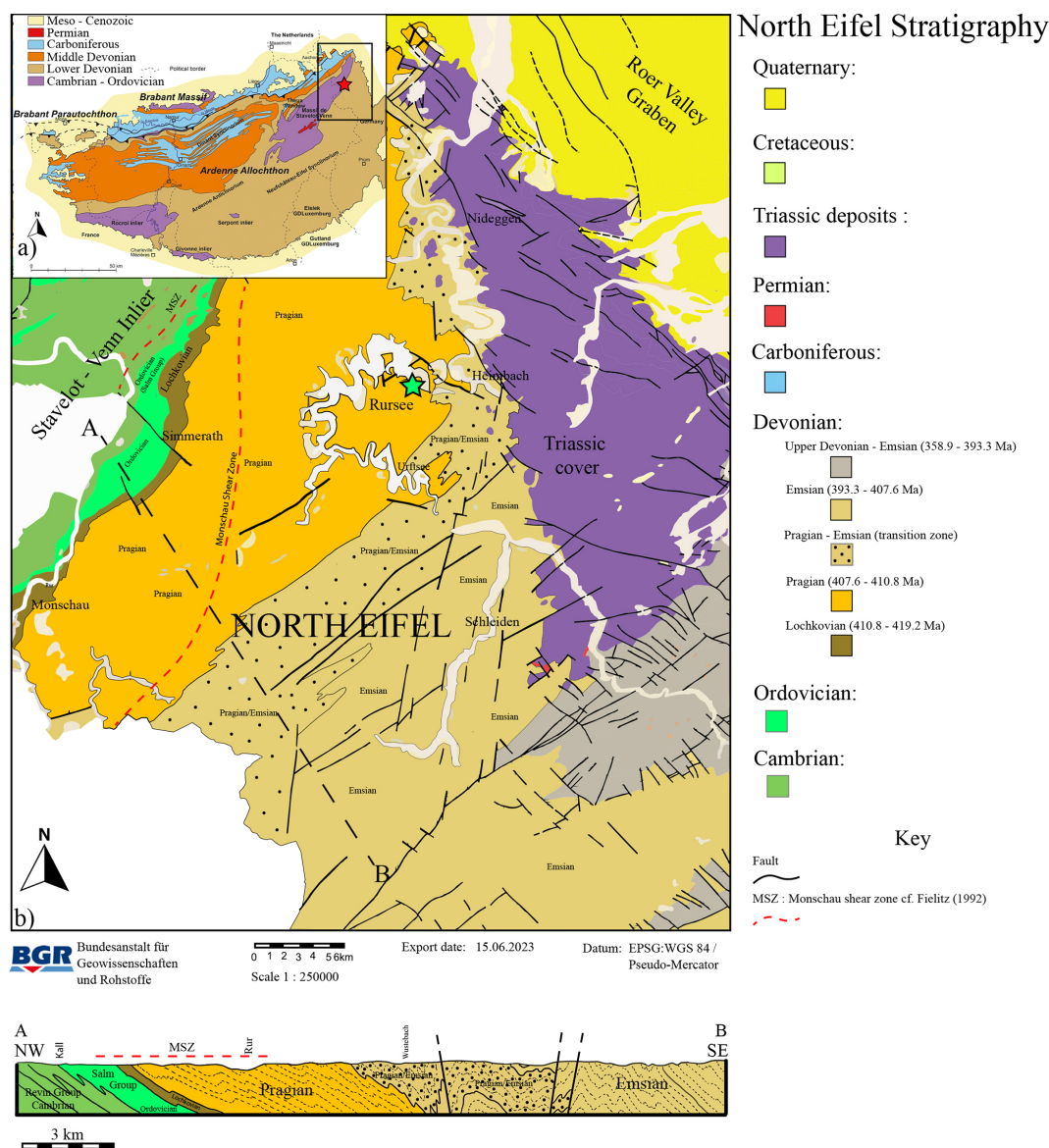


Figure 1. (a) Geological map with the Variscan frontal zone in the Ardennes–Eifel region (study area marked with a red star). (b) Geological map of the North Eifel region (modified after Ribbert et al., 1992; Van Noten et al., 2011). The Lower Devonian layers overlay metamorphic deposits of the lower Palaeozoic Stavelot–Venn inlier. These layers have been locally distorted in the Monschau Shear Zone (MSZ), as documented by Fielitz (1992). Triassic sediments overlay the Lower Devonian layers in the eastern region. The sample location, indicated by a green star, is situated next to the Rursee reservoir, which is near the Schwammenauel dam. Below, the cross-section illustrates the continuous northwest–southeast-trending overturned folds that characterize the North Eifel zone.

1997; Schneider and Haack, 1997; Glasmacher et al., 1998; Schneider et al., 1999; Chatziliadou and Kramm, 2009).

The $^{40}\text{Ar} / ^{39}\text{Ar}$ study targets the BNVs and BPVs (Fig. 2), which formed in low-grade metamorphosed (prehnite–pumpellyite facies) conditions as a result of the precipitates from warm fluids in fractures (Van Noten et al., 2008). The structural cross-cutting relationships between these quartz vein generations suggest that they originated from different geological events (Van Noten et al., 2008), revealing that BPVs are younger than BNVs. BNVs are mostly found

within the competent psammite and hardly occur in incompetent pelitic layers. This positioning suggests that BNVs formed during the early stages of the Variscan Orogeny, associated with the final burial phases of the Ardennes–Eifel basin (Sintubin et al., 2000; Urai et al., 2001; Van Noten et al., 2008, 2009).

In contrast, BPVs follow the strata between the psammatic and pelitic layers due to bedding-parallel slip caused by flexural folding during the Variscan Orogeny (Van Noten et al., 2008).

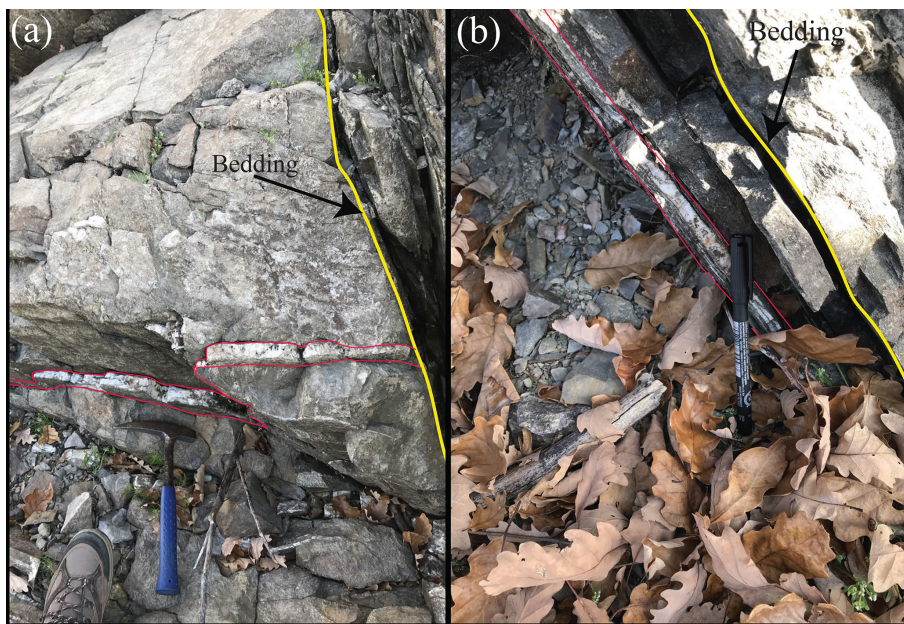


Figure 2. Images of studied outcrops from the Rursee area. The image in (a) presents the bedding-normal veins (red lines), while panel (b) shows the bedding-parallel veins (red lines). Yellow lines indicate the bedding in both images.

2 Material and methods

2.1 Quartz and inclusions in quartz minerals

In total, seven samples of different veins (three BNVs and four BPVs) were collected from the Rursee outcrop for $^{40}\text{Ar}/^{39}\text{Ar}$ analysis (Table 1). Both vein types mainly consist of elongated-fibrous milky quartz grains that exhibit syntaxial growth, whereby the growth starts from the wall of the veins towards the central part of the veins (Ramsay, 1986). The pelitic host rock consists of sericite, illite, white mica, and chlorite. Chlorite is abundant within the vein fractures and between the host rock and the vein wall.

Both quartz vein generations lack primary fluid inclusions in the crystal growth zones and contain pseudo-secondary and secondary fluid inclusions (FIs) ($< 10\ \mu\text{m}$) (Van Noten et al., 2011) in the sealed microcracks being perpendicular to crystal elongation (Fig. 3). The Rursee quartz vein samples yield average fluid inclusions homogenization temperatures (minimum trapping temperature, T_h) of $\sim 135 \pm 25$ and $\sim 160 \pm 20\ ^\circ\text{C}$ for BPV and BNV, respectively, with salinities of 3.5–8 eq. wt % NaCl. The T_h values of pseudo-secondary and secondary fluid inclusions cover an equally broad range of 110–180 $^\circ\text{C}$ (Van Noten et al., 2011).

2.2 Mineral separation

Before $^{40}\text{Ar}/^{39}\text{Ar}$ analysis, mineral separation was conducted at Vrije Universiteit Amsterdam (VU; The Netherlands). The bulk vein samples were crushed, washed, and cleaned in an ultrasonic bath for at least 1 h to remove the ad-

hering host rock contaminants from quartz grains. The samples were sieved into 250 and 500 μm fractions and dried in an oven at 60 $^\circ\text{C}$. The samples were further separated by a custom-made system using an overflow centrifuge with conventional heavy liquids based on IJlst (1973) and Frantz magnetic separation (Porat, 2006). We used heavy liquids with a density of 2.62 and 2.64 g cm^{-3} to obtain a fluid inclusion-rich fraction of quartz grains ($\rho = 2.62\text{--}2.64\ \text{g cm}^{-3}$). The fraction was rinsed with acetone, dried, and further sieved to separate the 400–500 μm grain size range. From this fraction, only the purest quartz grains were handpicked under a binocular microscope for $^{40}\text{Ar}/^{39}\text{Ar}$ dating.

2.3 $^{40}\text{Ar}/^{39}\text{Ar}$ stepwise crushing

Fluid-rich quartz grains (400–500 μm ; 2.62–2.64 g cm^{-3}) were carefully selected under a binocular zoom microscope, and a quantity of 200–270 mg of material was packed in aluminium foil and placed in 20 mm i.d.–22 mm o.d. aluminium cups. Drachenfels (DRA-2) sanidine standard was loaded after each three samples to monitor the neutron flux. The samples were irradiated at Oregon State University (USA) using the CLICIT (Cadmium-Lined In-Core Irradiation Tube) facility for 12 h (batch VU123). After irradiation, standards were placed in 2 mm copper planchet holes for single grain fusion analysis and pre-baked in a vacuum at 250 $^\circ\text{C}$. The samples were then placed in an ultra-high vacuum system; baked at 120 $^\circ\text{C}$; and connected with hot NP10 and ST172 getters, a Ti getter sponge at 400 $^\circ\text{C}$, and a cold trap at $-70\ ^\circ\text{C}$. The standards were fused with a Synrad 48-5 CO_2 continuous-wave laser fusion system.

Table 1. Summary of ⁴⁰Ar / ³⁹Ar age spectra, including inverse isochron data of all analysed quartz samples. The maximum apparent ages of the late converging section and inverse isochron selected, as discussed in the text, are highlighted in bold, with an asterisk marking those used for geological interpretation.

		Rursee, outcrop near Schwammenauel dam (Germany)									
		Quartz veins									
		Quartz									
Sample ID		Rursee 1a BNV	Rursee 1b BNV	Rursee 2 BPV	Rursee 2.1 BNV	Rursee 3 BPV	Rursee 4 BPV	Rursee 5 BNV	Rursee 6 BPV		
Rock type		Rursee									
Mineral		Quartz									
Sample ID Ar		R01a	R01b	R02	R021	R03	R04	R05	R06		
GPS coordinate		Lat.: 50.63378406 6.44191402		Lat.: 50.63377933	Lat.: 50.63388498	Lat.: 50.63418108	Lat.: 50.6344143	Lat.: 50.63367794	Lat.: 50.63392217		
			Long.:	Long.: 6.44190753	Long.: 6.44184657	Long.: 6.44176707	Long.: 6.4418217	Long.: 6.44201891	Long.: 6.44181953		
Grain size (µm)					400–500						
Density (g cm ⁻³)					2.62–2.64						
Max. apparent age (Ma)		2844	84*	97*	145	560	129	193	201		
±2σ analytical error + J error		±88	±1	±2	±7	±45	±5	±14	±6		
±2σ full external error		±96	±2	±3	±8	±47	±6	±15	±7		
MSWD (app. age)		42.8	1.6	3.3	4.3	6.1	5.4	2	0.4		
K / Ca		0.32	1.54	14.28	5.33	0.285	3.21	0.75	3.48		
⁴⁰ Ar / ³⁶ Ar inverse isochrone intercept		3874	326	858	258	329	311	289	243		
±2σ analytical error + J error		±7285	±51	±860	±38	±183	±6	±29	±181		
Inverse isochrone age		–	74	81	216	399	117*	259	26		
±2σ analytical error + J error		±5770	±16	±225	±51	±425	±7	±129	±177		
±2σ full external error		±5770	±16	±225	±51	±425	±8	±129	±177		
n / n _{tot} (n: number of analyses included weighted mean, n _{tot} : total number of analysis)		22/67	11/83	4/67	19/73	4/62	4/75	9/64	3/75		
MSWD (iso. age)		14.5	1.6	0.2	3.8	8.8	0.9	2.2	0.5		

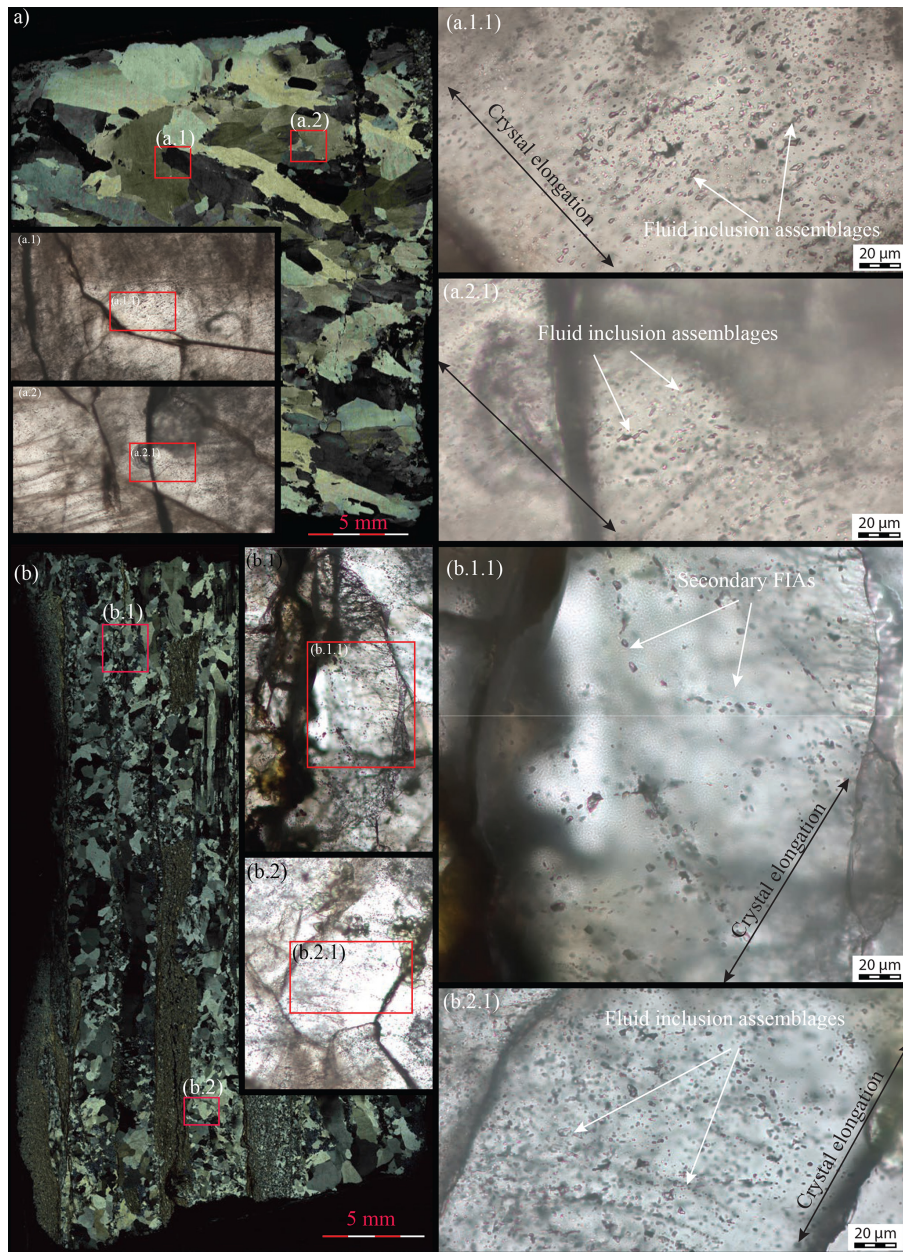


Figure 3. Fluid inclusions in quartz veins under optical microscopy. **(a)** Image of BNVs under crossed polarizer light microscopy. Both (a.1.1) and (a.2.1) are the zoomed-in view of the images in (a.1) and (a.2), respectively, indicating pseudo-secondary fluid inclusions. **(b)** Crossed polarizer images of the BPV sample under microscopy. The images in (b.1.1) and (b.2.1) are areas focused on secondary and pseudo-secondary fluid inclusion (respectively), which are zoomed-in views of the images in (b.1) and (b.2), respectively. The white arrows represent the fluid inclusion assemblages (FIAs). Both generations of quartz veins bear FIAs in sealed microcracks rather than in crystal growth zones.

The samples were crushed in an in-house developed and built crusher consisting of a stainless-steel tube (height: 18 cm, outer diameter: 1.8 cm) that has a spherical curve on its interior base and a magnetic stainless-steel pestle (height: 5 cm, diameter: 1.6 cm, weight: ~ 69.5 g) with rounded tips with a slightly narrower outer radius. These geometries allow optimization of the impact on the sample while crush-

ing. Once a split of the sample (~ 30 mg of quartz grains) was loaded into the crusher tube, the pestle was carefully re-located to the bottom of the tube to avoid crushing the sample. The crush tube, the pestle, and the sample were baked overnight at 250°C . The pestle was dropped into a free-fall state using an external electromagnet with a frequency of 1 Hz controlled by an adjustable power supply and pulse

generator to crush the sample. The pestle was dropped from a height of ~ 3 , ~ 4 , or ~ 5 cm in vacuo. Subsequently, the gases emitted from fluid inclusions in the fragmented quartz sample were analysed. To obtain a sufficient amount of argon in the mass spectrometer, the number of pestle drops per extraction step and drop height were systematically increased during the experiment, with a maximum of 999 drops per analysis (in total, $\sim 40\,000$ cumulated pestle drops per experiment).

The gas released from the samples and standards was analysed isotopically using a ThermoFisher Scientific Helix MC+ mass spectrometer. The Helix MC+ mass spectrometer is a 5-collector channel instrument, equipped with a total of 10 collectors, a Faraday (Far) collector optionally fitted with a 10^{12} or 10^{13} Ohm resistor amplifier, and a compact discrete dynode secondary electron multiplier (CDD-SEM) collector on each collector channel. Five collectors can be used at the same time to simultaneously collect the beam intensity signals of the five isotopes of argon. The H2 Faraday collector is employed to detect ^{40}Ar using a 10^{13} Ohm amplifier. Similarly, the H1 CDD collector is used for the measurement of ^{39}Ar (H1 Faraday was used for the runs on the DRA-2 sanidine standard because of the higher ^{39}Ar signal), the AX CDD collector for ^{38}Ar , the L1-CDD collector for ^{37}Ar , and the L2 CDD collector for ^{36}Ar .

Line blanks were measured after every three to four unknowns and subtracted from the succeeding sample data. Gain calibration is done by correcting for gain relative to the beam intensity measured on the AX CDD, using measurements of ~ 50 fA (^{40}Ar -measured beam intensities) pipettes of air on each cup, and mass discrimination corrections are made by measuring a series of ~ 400 fA (^{40}Ar -measured beam intensities) air pipettes roughly every 12 h. Raw data were processed using the ArArCALC software (Koppers, 2002). Ages are calculated relative to Drachenfels (DRA-2) sanidine of 25.552 ± 0.078 Ma (Wijbrans et al., 1995), which was recalibrated against Fish Canyon Tuff sanidine of 28.201 ± 0.023 Ma (Kuiper et al., 2008). The decay constants of Min et al. (2000) are used. The atmospheric $^{40}\text{Ar}/^{36}\text{Ar}$ ratio of 298.56 ± 0.31 is based on Lee et al. (2006). The correction factors for neutron interference reactions are $(2.64 \pm 0.02) \times 10^{-4}$ for $(^{36}\text{Ar}/^{37}\text{Ar})_{\text{Ca}}$, $(6.73 \pm 0.04) \times 10^{-4}$ for $(^{39}\text{Ar}/^{37}\text{Ar})_{\text{Ca}}$, $(1.21 \pm 0.003) \times 10^{-2}$ for $(^{38}\text{Ar}/^{39}\text{Ar})_{\text{K}}$, and $(8.6 \pm 0.7) \times 10^{-4}$ for $(^{40}\text{Ar}/^{39}\text{Ar})_{\text{K}}$. Gain correction factors and their standard errors (± 1 SE) are 1.00162 ± 0.00028 for H2 Far, 0.97963 ± 0.00021 for H1 CDD, 0.99921 ± 0.00027 for L1 CDD, and 0.96163 ± 0.00064 for L2 CDD for data measured in 2022 (R2.1) and 1.00465 ± 0.00031 for H2 Far, 0.97033 ± 0.00027 for H1 CDD, 0.99824 ± 0.00033 for L1 CDD, and 0.96309 ± 0.00070 for L2 CDD for data measured in 2023 (R1–R6). The K/Cl ratios are calculated by $\text{K}/\text{Cl} = \beta \times ^{39}\text{Ar}/^{38}\text{Ar}$, with $\beta = 0.06$ derived from $\text{K}/\text{Cl} = \sim 18.7$ in GA1550 and $^{39}\text{Ar}_{\text{K}}/^{38}\text{Ar}_{\text{Cl}} = \sim 316$ for a 12 h irradiation

at the OSU Triga CLICIT facility. All errors are quoted at the 2σ level and include all analytical uncertainties (Table 1).

Please note that it is impossible to directly correct the crushing blank because we cannot perform the exact experiment without crushing sample material. We tested the blanks for each tube without sample material, following the identical procedures as for real experiments. With this approach, we have direct metal-to-metal contact during pestle drops, which might not be representative of a real sample. We did observe a substantial increase in background, with a higher number of drops and a higher drop level. Notably, the composition of this blank is similar to that of atmospheric argon. Therefore, we follow the approach that the ^{40}Ar signal derived from the line blank (measured every three to four unknowns where we mimic the sample experiment but without the crushing/pestle drops) is subtracted from the measured ^{40}Ar intensity. The real blank has an atmospheric $^{40}\text{Ar}/^{36}\text{Ar}$ ratio and is incorporated in the air corrections, leading to a lower radiogenic $^{40}\text{Ar}^*$ if the real blanks are relatively high.

2.4 Electron probe microanalysis

Quartz grains of sub-samples that were analysed for $^{40}\text{Ar}/^{39}\text{Ar}$ were mounted in epoxy resin and carbon-coated for the JEOL JXA-8530F Hyperprobe field emission electron probe micro-analyser (EPMA) at Utrecht Universiteit (UU; the Netherlands) to define the elemental compositions of (1) the host quartz; (2) minerals that are present in fluid inclusions, filled cavities, or fractures; and (3) mineral inclusions in the quartz. For this analysis, an accelerating voltage of 15 kV and a beam current of 8 nA for host rock (quartz) and 7 nA for mineral inclusions are used with beam sizes of 10 and 1 μm , respectively. The elements analysed are Si, Ti, Al, Fe, Mn, Ca, Na, K, P, Cl, F, Ba, and Zr. The data are calibrated using Icelandic rhyolite glass (ATHO-G) and basalt glass (KL2-G) standards that were measured with a beam size of 10 μm multiple times both before and after measurements of the samples.

3 Results

The age spectra of the in vacuo stepwise crushing of the quartz samples are plotted in Fig. 4. All samples show typical release patterns with unrealistically old apparent ages (> 6 Ga) in the initial 10 % of $^{39}\text{Ar}_{\text{K}}$ released. Note that samples Rursee 1a BNV and Rursee 1b BNV are measured in two different experiments on subsets from the same irradiated sample, yielding different results. A lighter pestle (68 g) has been used for the sample Rursee 1a BNV than for sample Rursee 1b BNV (69.5 g) and all other samples.

The apparent ages of the spectra in samples Rursee 1b BNV, Rursee 2 BPV, Rursee 2.1 BNV, and Rursee 4 BPV exhibit a gradual decrease in age over the next 10 %–40 % of $^{39}\text{Ar}_{\text{K}}$ released, eventually stabilizing at a more or less consistent maximum apparent age from ~ 80 % $^{39}\text{Ar}_{\text{K}}$ to

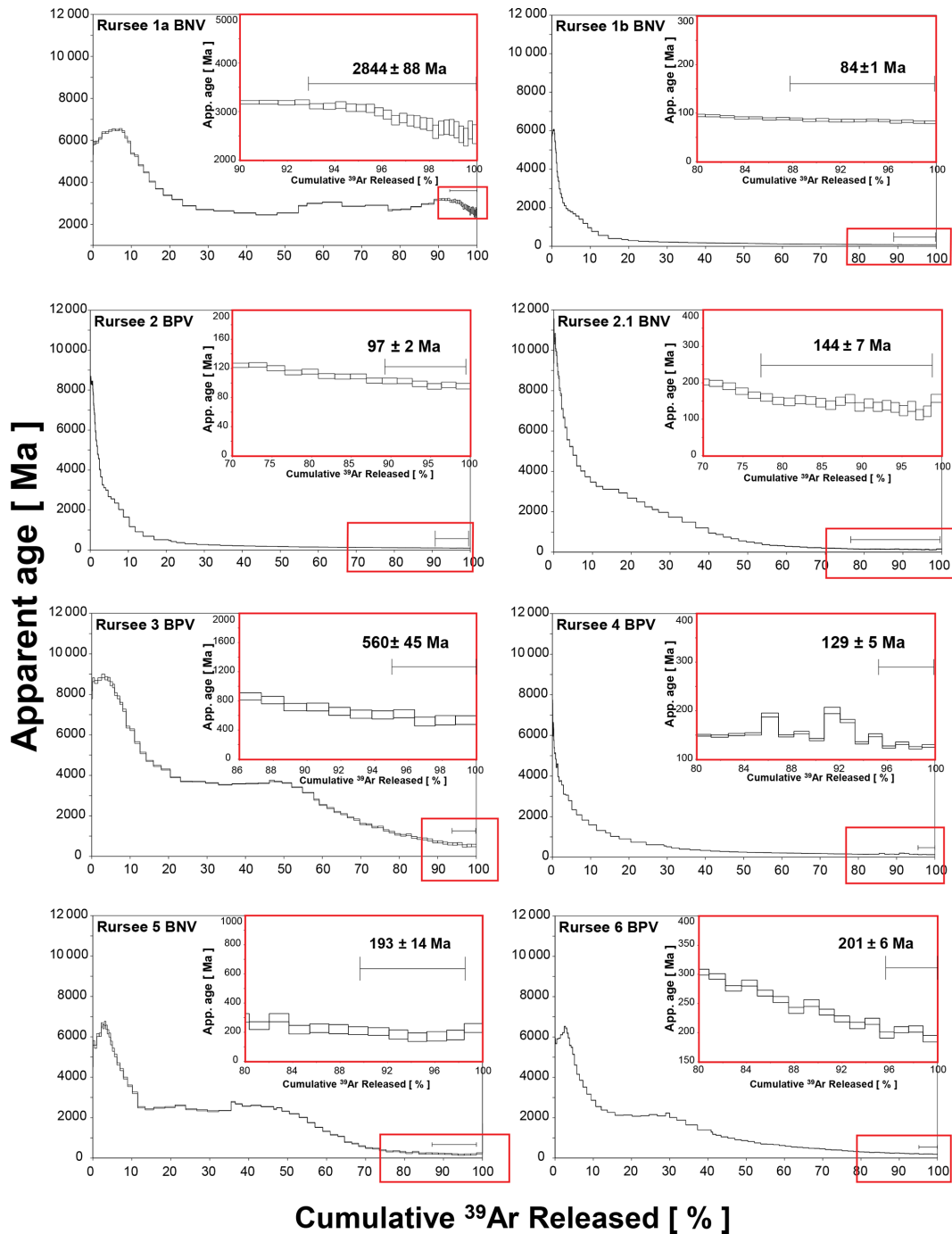


Figure 4. The apparent late converging section age of all quartz vein experiments. The red boxes focus on the last part of the age spectra, where apparent ages are more or less stable.

$\sim 100\%$ $^{39}\text{Ar}_K$. Rursee 3 BPV, Rursee 5 BNV, and Rursee 6 BPV show comparable behaviour with, after the initial old apparent ages, a decrease in a maximum apparent age to an “early converging section” from $\sim 15\%$ to $\sim 40\%$ $^{39}\text{Ar}_K$ released, followed by a gradual decrease in apparent age and a more or less uniform apparent age in the $> 80\%$ released $^{39}\text{Ar}_K$ part of the spectrum. For these early converg-

ing sections, we arrive at averaged maximum apparent ages of ~ 84 Ma for Rursee 1b BNV, ~ 97 Ma for Rursee 2 BPV, ~ 117 Ma for Rursee 4 BPV, ~ 216 Ma for Rursee 2.1 BNV, ~ 190 – 200 Ma for Rursee 5 BNV and Rursee 6 BPV, and ~ 560 Ma for Rursee 3 BPV. The maximum apparent ages of Rursee 2.1 BNV and Rursee 4 BPV correspond to the inverse isochron maximum apparent ages; however, due to signifi-

cant uncertainty, the maximum apparent ages of other samples were obtained from the average “late converging section” age (Table 1).

The inverse isochrons (Fig. 5) confirm that the first part of all experiments is heavily affected by excess argon ($^{36}\text{Ar}/^{40}\text{Ar}$ ratios are much lower than atmospheric composition), followed by an increase in $^{36}\text{Ar}/^{40}\text{Ar}$ and $^{39}\text{Ar}/^{40}\text{Ar}$ ratios and clustering of data points on the reference line. We derived maximum apparent ages from the data points that cluster along the reference line in the isochrons in the final part of the age spectra. There is no systematic maximum apparent age difference between BNV and BPV.

All quartz samples release argon during in vacuo stepwise crushing with different isotopes of argon contributing to the gas release at different stages of the experiment. Figure 6 shows, for each step, the percentage (relative to the total amount) of a specific isotope released through the experiment. All quartz samples are characterized by a release of most of the $^{36}\text{Ar}_{\text{air}}$ in the first 20 steps. $^{40}\text{Ar}^*$ and $^{38}\text{Ar}_{\text{Cl}}$ follow the pattern of $^{36}\text{Ar}_{\text{air}}$. The $^{39}\text{Ar}_{\text{K}}$ generally increases after the first 20 analysing steps (~ 790 pestle drops from 3 cm height). At steps 30–35, we observe fluctuations in the data. These shifts are artefacts caused by increasing the drop height (from 3 to 4 cm at \sim step 30 and from 4 to 5 cm at \sim step 35) and adjusting the number of pestle drops. To prevent high signals, we started with a relatively low number of pestle drops at a higher drop height, yielding low signals, as observed as two troughs at \sim step 30 and \sim step 35 in all experiments. All quartz samples are low in $^{36}\text{Ar}_{\text{air}}$, $^{38}\text{Ar}_{\text{Cl}}$, and $^{40}\text{Ar}^*$ at the end of analysis compared to their total release. For $^{40}\text{Ar}^*$, we still measure a small, reliable signal, but this is obscured in Fig. 6 due to the high signals in the first steps since we plot percentages of the total released ^{40}Ar per experiment. Note that huge amounts of excess ^{40}Ar (as part of the $^{40}\text{Ar}^*$ signal) are released in the initial steps of the experiment and dominate the total percentage.

4 Discussion

During in vacuo stepwise crushing, the release of argon isotopes from the samples follows systematic patterns. The challenge is to link this release of argon from the samples to the different potential reservoirs of K and, as a next step, the geological meaning of the age and elemental ratios of K/Cl and Ca/Cl. Here, we first discuss potential issues related to the analytical quality of the data. Next, we discuss potential reservoirs of K and subsequently $^{40}\text{Ar}^*$ that need to be considered, evaluating the maximum apparent ages and their wider implications.

4.1 Data quality

4.1.1 Rursee 1a and 1b BNV

We speculate that for the Rursee 1a BNV experiment, we sampled a smaller part of the argon reservoirs in the quartz minerals comparable to the first 10 % of the spectrum of Rursee 1b BNV. This is corroborated by the fact that for Rursee 1a BNV, 46 mg of quartz released 12.7 fA $^{39}\text{Ar}_{\text{K}}$ (0.3 fA mg^{-1} quartz), while for Rursee 1b BNV, 89.1 fA was released from 25 mg of quartz (3.6 fA mg^{-1} of quartz). We therefore do not further discuss the results of Rursee 1a BNV but note that sample heterogeneity might also have contributed to this difference.

4.1.2 Impact of blank correction

The blank correction procedure likely does not impact the weighted mean age computation; however, it does influence the $^{40}\text{Ar}/^{36}\text{Ar}$ intercept of the inverse isochron. This is only the case when the regression line has a non-radiogenic intercept that differs from the atmospheric $^{36}\text{Ar}/^{40}\text{Ar}$. When the intercept is within the error overlapping with the atmospheric ratio, the blank correction only causes the point to move along the regression line, which comes out of the discussion below. We described our blank correction procedure in methods (Supplement file S1). The fact that we cannot mimic the dropping of the pestle when a sample is present in the tube limits how well we can determine the blank during the experiments. The blank tends to increase with a higher number of pestle drops, but the composition of this blank is atmospheric. For the test of the blank, we used quartz glass fragments to mimic zero-age minerals, as a blank determination using metal-on-metal impacts was considered to be an unrealistic scenario. As a next test, we artificially increase the ^{40}Ar blank (and thus the ^{36}Ar blank) assuming atmospheric composition. If the data are located on the mixing line between radiogenic and atmospheric argon, this should not affect the isochron apparent age (pink part – final stage in Figs. 5 and 11). We tested this for sample Rursee 1b BNV with an apparent age of ~ 88 Ma. The $^{40}\text{Ar}/^{36}\text{Ar}$ intercepts increase with increasing blank values, and the weighted mean late converging section ages change with a maximum of 2.5 Ma in the chosen example. We therefore conclude that the isotopic ages remain largely unaffected by varying the amounts of atmospheric argon of the blanks. Note that if the isochron is not a mixing line between radiogenic and atmospheric argon (e.g. blue and green parts in Figs. 5 and 11), this assumption is incorrect. The $^{40}\text{Ar}/^{36}\text{Ar}$ intercept is then pulled away from the real $^{40}\text{Ar}/^{36}\text{Ar}$ composition in the direction of the atmospheric $^{40}\text{Ar}/^{36}\text{Ar}$ intercept. Consequently, the intercept with the inverse isochrons' x axis (and thus age) will also be affected.

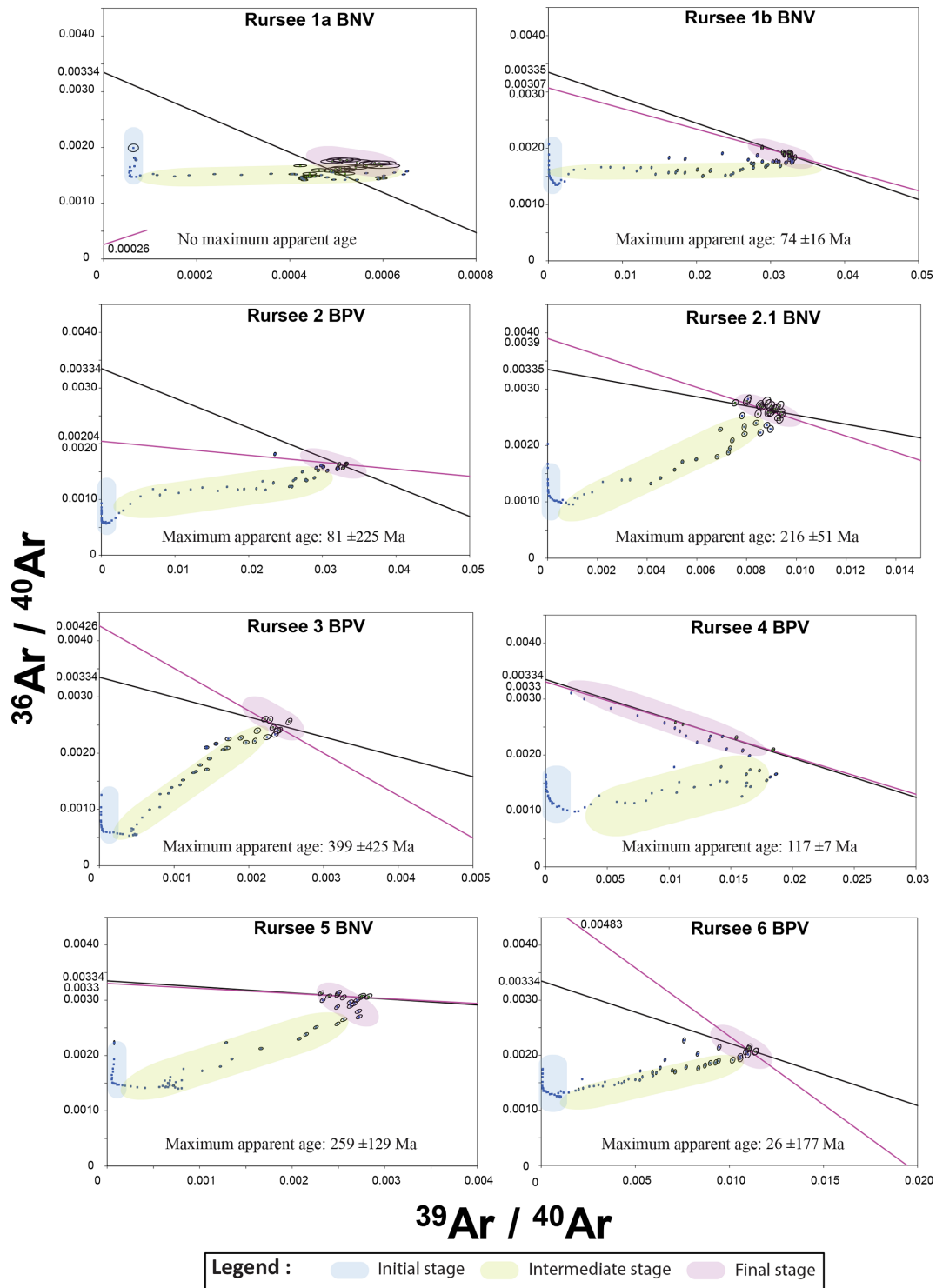


Figure 5. Inverse isochrons of all quartz vein samples. The black line corresponds to a regression where the $^{40}\text{Ar}/^{36}\text{Ar}$ intercept with the vertical is fixed at the ratio of atmospheric argon, and hence its radiogenic intercept corresponds to the age obtained from a regression of the corresponding steps in the age spectrum, whereas the pink line represents a regression without this restriction, providing us with information on the actual $^{40}\text{Ar}/^{36}\text{Ar}$ ratio of non-radiogenic components in the fluid mixture.

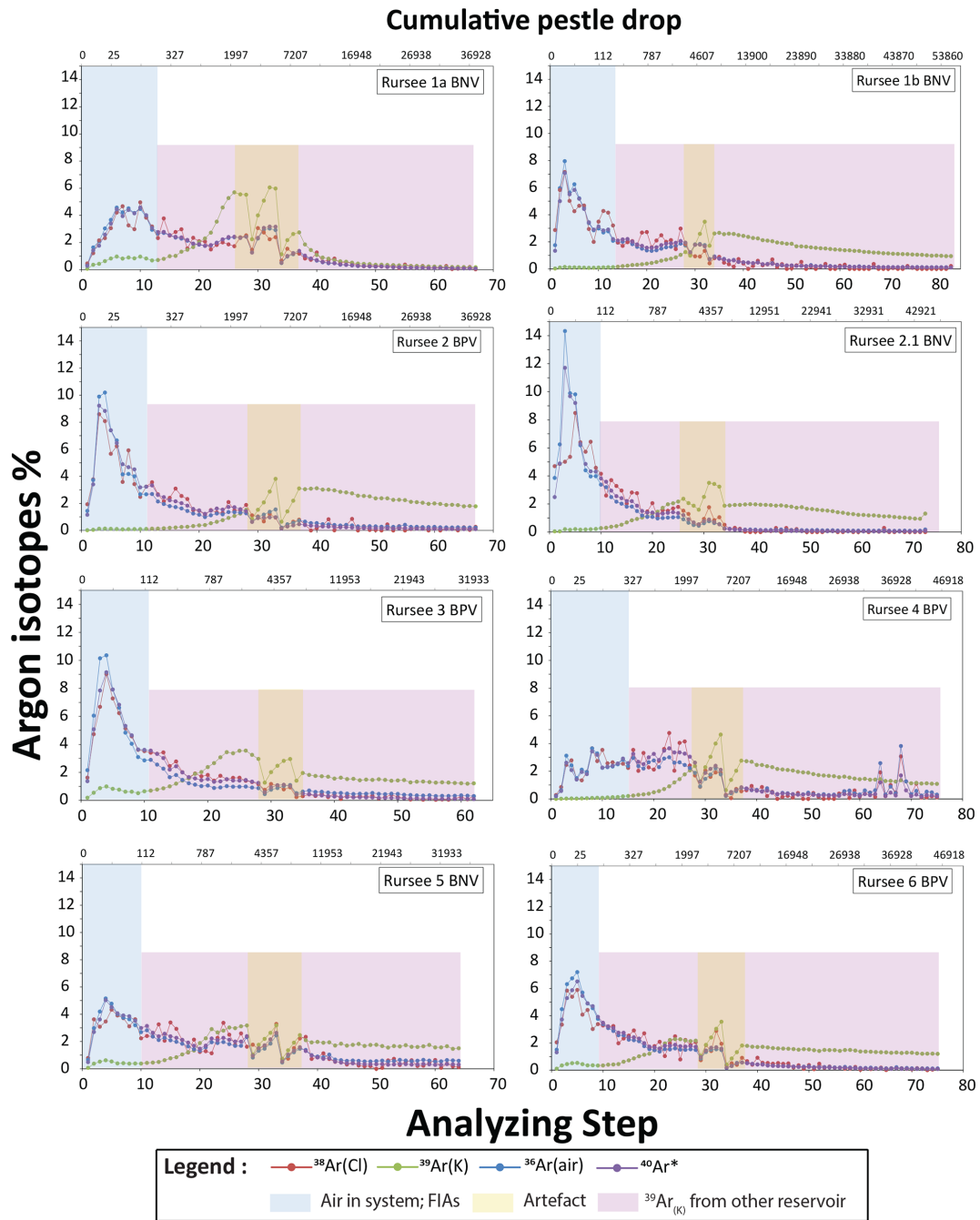


Figure 6. Released argon isotopes per analysing step relative to their total release. Note that the data are expressed against the analysing steps instead of the crushing steps, and that the upper x -axis scaling (cumulative pestle drops) is neither linear nor logarithmic (non-continuous scaling).

4.1.3 Recoil artefacts

Recoil artefacts occur when ^{37}Ar and ^{39}Ar , which are formed from K and Ca isotopes, form with kinetic energy. As a result, they can travel from their original sites to other sites, potentially even into the adjacent phase (Turner and Cadogan, 1974; Foland, 1983; Lo and Onstott, 1989; Féraud and Courtillot, 1994; Baksi, 1994; Onstott et al., 1995; Villa, 1997).

However, this phenomenon is assumed to have a smaller impact than the blank correction.

4.2 Potential reservoirs of K

To date, three main hypotheses have been debated about the origin of the released argon in a stepwise crushing experi-

ment. The first group (Qiu and Wijbrans, 2006, 2008; Bai et al., 2019) suggests that progressive crushing releases gases mainly from fluid inclusions and therefore represents fluid inclusions maximum apparent ages. Additionally, there is a possibility of argon releasing within K minerals by prolonged crushing when the grain sizes are reduced to tens of nanometres (Bai et al., 2019).

The second group (e.g. Kendrick and Phillips, 2009) discusses the possibility of K-bearing mineral inclusions within the inclusion cavity and/or in microcracks serving as argon reservoirs in the later crushing stages. Obtained maximum apparent ages therefore represent mineral closure ages or a mixture of fluid inclusions and mineral inclusion ages. Accordingly, the gas release sequence under sufficient crushing progresses from microcracks to secondary fluid inclusions, followed by primary fluid inclusions, and finally to micro- to nanometre-sized minerals (Bai et al., 2022).

In addition, the third potential source of potassium in the minerals might be the presence of K^+ in the crystal lattice, which was postulated for zeolites (Kendrick et al., 2011) but could also work for feldspars but may be less of an issue in nominally potassium-free minerals such as quartz (or garnet), which is representative of the formation age of veins. Hydrothermal quartz veins, characterized by their substitution in the crystal structure, have been studied by Weil (1984) and Götze et al. (2021). These studies indicate that Si^{4+} derived from hydrothermal quartz veins can be substituted by other ions such as Al^{3+} , Ga^{3+} , Fe^{3+} , B^{3+} , Ge^{4+} , Ti^{4+} , and P^{4+} . Al^{3+} usually replaces Si^{4+} since it is found in significant amounts ($\sim 300\text{--}700$ ppm) in quartz, based on EPMA data. Additionally, small numbers of monovalent ions such as K^+ may fill empty spaces in the crystal structure, serving as charge balancers for trivalent substitutional ions such as Al^{3+} (Bambauer, 1961; Kats, 1962; Perny et al., 1992; Stalder et al., 2017; Potrafke et al., 2019). However, Jourdan et al. (2009) postulated that substitutions of these components may be so minor that they are even undetectable using a secondary ion mass spectrometer (SIMS). Furthermore, it is important to note that not all hydrothermal sources or quartz minerals have this particular form of substitution (Jourdan et al., 2009).

Apart from these potential $^{39}\text{Ar}_{\text{K}}$ reservoirs above, detrital minerals (e.g. mica present in the surrounding pelitic rock) that might be trapped by the quartz veins during the growth may also contribute to the obtained maximum apparent ages.

4.2.1 Identification of different K reservoirs in the Rursee quartz samples

During in vacuo stepwise crushing, the release of argon isotopes from the samples follows systematic patterns. In this study, we aim to connect this release to the sequential contributions of different reservoirs of K and, consequently, argon from the Rursee samples. The release patterns of $^{36}\text{Ar}_{\text{air}}$,

$^{38}\text{Ar}_{\text{Cl}}$, $^{39}\text{Ar}_{\text{K}}$, and $^{40}\text{Ar}^*$ (Fig. 6) for all quartz vein samples may originate from multiple existing argon reservoirs.

Depending on the size ($< 10\ \mu\text{m}$), location, and generation of fluid inclusions, they may contribute successively to the argon release patterns in the early or middle stage of stepwise crushing. Figure 6 reveals that the concentration of $^{39}\text{Ar}_{\text{K}}$ increases throughout the process of in vacuo stepwise crushing, while the concentration of other argon isotopes decreases. This suggests that K-containing reservoirs were not opened in the first part of the experiment. The release patterns of $^{39}\text{Ar}_{\text{K}}$ can be categorized into two distinct groups during stepwise crushing.

The *first group* of samples shows a small initial release in the early stages. This is followed by a drop around the 10th step, then an increase from the ~ 10 th to ~ 35 th step, and finally a gradual decrease (Rursee 3 BPV, Rursee 5 BNV, and Rursee 6 BPV).

The *second group* does not have the $^{39}\text{Ar}_{\text{K}}$ release in the steps 1–10 but after that it shows a similar pattern to the first group, gradually increasing until about the 35th step and then gradually decreasing (Rursee 1b BNV, Rursee 2 BPV, Rursee 2.1 BNV, and Rursee 4 BPV).

The continuous rise in $^{39}\text{Ar}_{\text{K}}$ levels after ~ 10 steps in both sample groups suggests that the gas release process can be divided into at least two phases. Initially, during the first ~ 10 steps, $^{39}\text{Ar}_{\text{K}}$ is emitted from fluid inclusions in microcracks (secondary fluid inclusions). From steps ~ 10 to ~ 70 , the release happens as a result of the mixing of potential pseudo-secondary fluid inclusions (~ 10 th to ~ 15 th steps), mineral inclusions, and/or the crystal lattice of quartz veins. This interpretation is supported by the K / Cl correlation plots (Fig. 7), which show a consistently lower K / Cl ratio until the ~ 10 th step.

From the 10th to the 15th K / Cl ratio, it reaches ~ 1 with a steep rise for all quartz samples, and later (from the ~ 20 th step) this ratio continues to increase steeply for the second group of samples, while it shows a less pronounced increase for the first group of samples.

The lower K / Cl ratio may be attributed to the presence of Cl and a lack of or limited amounts of K in combination with relatively constant low salinity levels (3.5–8 eq. wt % NaCl) inside the fluid inclusions, which are likely to be opened in the early phase. After most fluid inclusions have been mechanically opened, the subsequent rapid increase in K (reflected by the $^{39}\text{Ar}_{\text{K}}$) and the steady decline in Cl (reflected by the $^{38}\text{Ar}_{\text{Cl}}$) occur throughout successive crushing steps and are reflected in the K / Cl ratio. Therefore, this increase is likely due to the exhaustion of the Cl-rich fluid inclusions along with the presence of minerals containing potassium and/or potassium from the crystal lattice of quartz that release their argon in the later crushing steps.

This approach to distinguish between fluid inclusions and other K reservoirs was first suggested by Kendrick et al. (2006, 2011): K / Cl ratios ≤ 1 are representative of fluid inclusions and K / Cl ratios > 1 for other sources. If

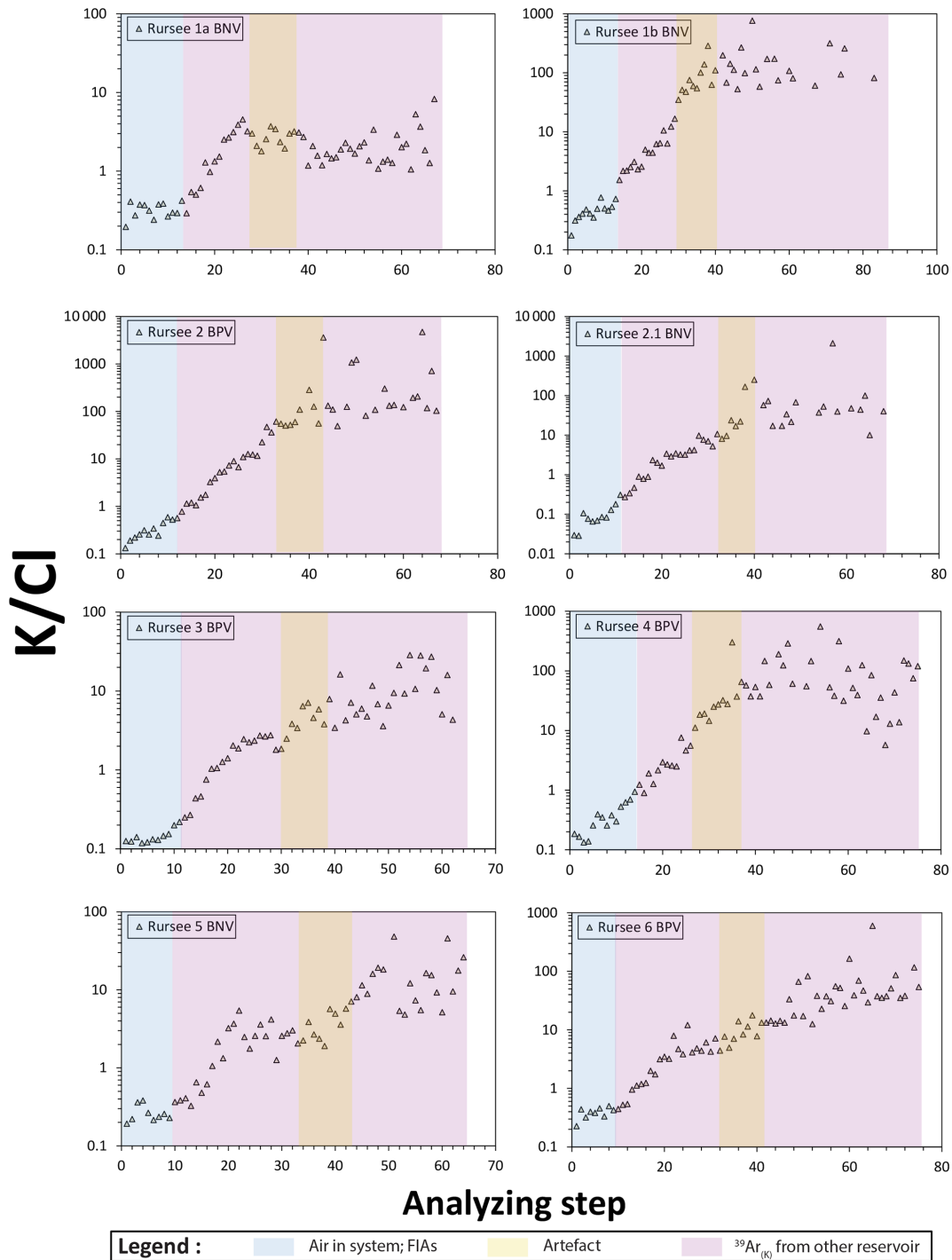


Figure 7. K / Cl ratios plotted against analysis steps for all quartz veins.

$K / Cl \leq 1$, the apparent age we measure is the oldest possible age for the fluid inclusions. In case $K / Cl > 1$, the obtained apparent age corresponds to the maximum apparent age of the trapped K-bearing mineral and/or K from the crystal lattice (Kendrick et al., 2006, 2011). In our samples, the K / Cl is greater than 1 after the first $\sim 15 \pm 3$ steps in all

quartz vein samples, indicating the presence of major K-related reservoir(s) other than fluid inclusions. It is worth noting that this is based on the assumption that there are no other K-bearing phases, such as KNO_3 , K_2SO_4 , or K_2CO_3 , rather than KCl dissolved in aqueous fluid inclusions. This assumption may be verified by Raman analysis (see Fig. A1),

which does not show significant peaks for these alternative K-bearing phases. However, the low peaks in $\sim 1080\text{ cm}^{-1}$ may be related either to K_2CO_3 or to interferences in relation to the epoxy background. Therefore, $\text{K} / \text{Cl} > 1$ suggests that K is related to the salinity of the fluid inclusions along with different K components (i.e. KCl and K_2CO_3). Alternatively, if there is interference from the epoxy background, it suggests that there should be at least one significant additional source present, which could include the crystal lattice of quartz and/or mineral inclusions within the quartz crystals and/or even microcracks.

4.2.2 K-bearing mineral inclusions

EPMA data (Table 2) from cleaned, hand-picked fluid-rich separated quartz grains indicate the presence of sericite, chlorite–sericite, and illite–sericite in the microfractures and cavities of fluid inclusion. The presence of such minerals (or mixtures) in the inclusion cavity and microfractures is also invisible under a binocular or petrographic microscope during the mineral separation and was confirmed captured using electron-backscattered imaging (Fig. 8). In thin sections of quartz, veins with the associated host rock, illite–sericite, and white mica are abundant in the surrounding pelitic layer of the Rursee formation (Fig. 9). These minerals that contain a significant amount of K_2O are also detected by an EPMA, in the separated quartz samples, especially in Rursee 2 BPV (see EPMA data, Table 2). High K concentrations ($\sim 8.8\text{ wt } \%$ K_2O) are likely related to intergrowth with sericite or a closely related mineral.

Petrographic analysis of thin sections of whole rock samples representing both vein generations (BPV and BNV) reveals a significant presence of chlorite located between the vein wall and host rock, as well as in fractures (Fig. 10). Although chlorite typically lacks K in its crystal structure, previous studies have reported trace amounts of K in chlorites (Pacey et al., 2020; Li et al., 2022).

4.2.3 K from crystal lattice and detrital minerals

EPMA analyses of the quartz matrix indicate that K concentrations in the crystal lattice are below the detection limit of $\sim 100\text{ ppm}$. A maximum K concentration of $\sim 100\text{ ppm}$ K (for example, 100 ppm K in Rursee 2.1 BNV) and a maximum apparent age of 144 Ma would result in $\sim 16000\text{ fA}$ $^{40}\text{Ar}^*$ when measured on our Helix MC+ mass spectrometer, which is a comparable amount of total $^{40}\text{Ar}^*$ released from K-bearing mineral inclusion. Given the large sample amount ($\sim 30\text{ mg}$), this would translate into a significant contribution of K from the crystal lattice of quartz. We therefore suggest that K in the crystal lattice may contribute to the observed $^{40}\text{Ar}^*$ signals (see calculation in the Supplement file S2).

In this study, argon molecules might also be derived from secondary minerals in cracks and embedded detrital minerals (e.g. mica from host rock). This interpretation aligns with the

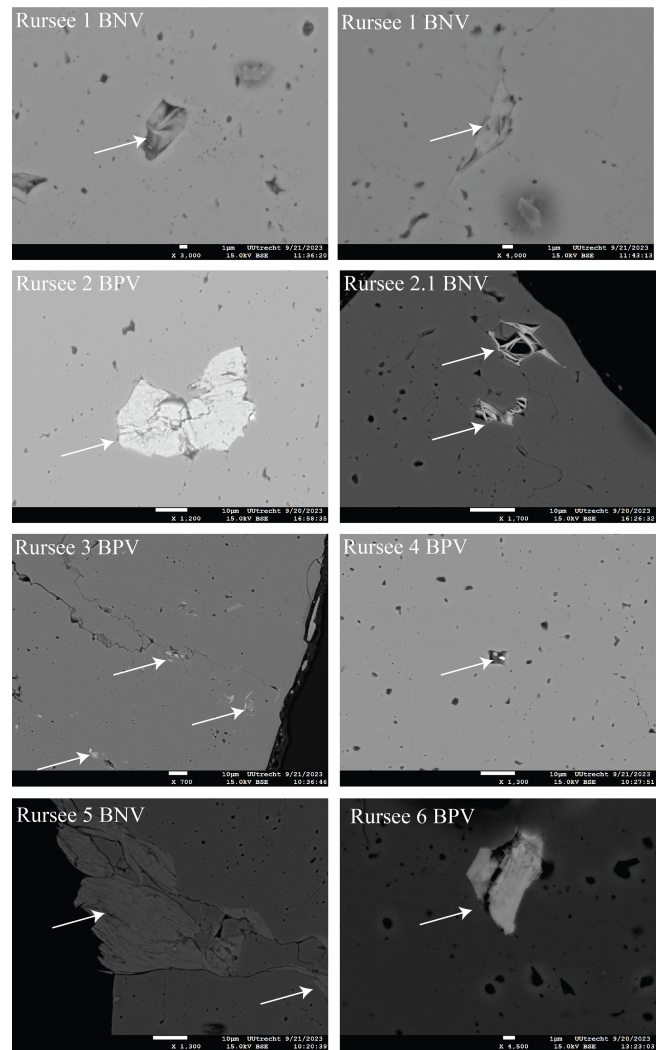


Figure 8. Backscattered electron images of mineral inclusions obtained by SEM. Secondary minerals (e.g. chlorite, sericite, and white mica as determined using an EPMA) occur in cavities and microfractures (white arrow) in fluid-rich quartz.

observation that the homogenization temperatures of fluid inclusions within the quartz veins are below the closure temperature for argon in detrital minerals. Under such conditions, the expected maximum apparent ages from K-bearing detrital minerals would correspond to pre-Variscan periods, reflecting the maximum apparent age of the deposits hosting the quartz veins, although the obtained maximum apparent ages are significantly younger in this study. Therefore, we infer that detrital minerals do not significantly contribute to the $^{40}\text{Ar}^*$ signals.

To summarize, during the first stages (until the $\sim 20\text{th}$ analysis steps) of the stepwise vacuo crushing, gases are likely released only from fluid inclusions (secondary and pseudo-secondary, as is also observed for fluid inclusion in garnets (Qiu and Wijbrans, 2006, 2008)). Huseynov et

Table 2. Elemental analysis of quartz grain, microcracks, and mineral inclusions in quartz vein samples under an EPMA.

EPMA analysis of mineral inclusions and microfractures of clean fraction of quartz veins' grain of Rursee samples (wt %).																			
Sample ID	Grain ID	SiO ₂	TiO ₂	Al ₂ O ₃	FeO	MnO	MgO	CaO	Na ₂ O	K ₂ O	P ₂ O ₅	Cl	F	BaO	ZrO ₂	O	H ₂ O	TOTAL	
Internal standard of UU	KL2-1	51.90	2.56	13.50	10.74	0.17	7.47	10.74	2.39	0.48	0.23	bdl	bdl	bdl	bdl	0.00	0.00	100.01	
		51.20	2.51	13.36	10.79	0.17	7.46	10.83	2.38	0.47	0.27	0.00	bdl	bdl	bdl	0.00	0.00	99.28	
		50.80	2.55	13.41	10.98	0.16	7.31	10.96	2.34	0.51	0.26	0.00	bdl	bdl	0.00	0.00	99.13		
Internal standard of UU	ATHO-1	75.73	0.21	12.23	3.28	0.11	0.11	1.67	3.85	2.73	0.02	0.05	0.06	0.09	bdl	0.00	0.00	100.10	
		75.61	0.24	12.44	3.47	0.12	0.13	1.63	3.73	2.78	0.05	0.05	0.03	0.00	0.02	0.00	0.00	100.29	
		75.69	0.28	12.30	3.43	0.12	0.11	1.60	3.78	2.81	0.02	0.03	0.04	0.04	0.10	0.00	0.00	100.35	
Rursee quartz veins	Rursee 1 BNV	B_1.01a	99.75	0.02	0.00	0.00	0.00	bdl	0.01	0.02	1.00	0.01	0.59	bdl	bdl	bdl	0.00	0.00	101.21
		B_1.02a	55.07	bdl	0.31	0.29	0.01	0.61	0.88	0.39	0.51	0.13	0.40	bdl	0.03	0.01	0.00	0.00	58.57
		B_1.03a	71.35	0.02	0.69	2.83	0.07	14.04	0.15	0.38	0.51	0.05	0.12	bdl	bdl	0.00	0.00	0.00	90.05
		B_1.03b	38.76	0.04	2.80	1.85	0.02	6.30	0.74	1.53	0.95	0.13	0.30	bdl	0.04	bdl	0.00	0.00	53.29
		B_1.06a	47.68	0.01	37.73	0.04	bdl	0.04	0.19	5.61	0.86	0.05	0.06	0.04	bdl	bdl	0.00	0.00	92.27
		B_1.06b	99.52	bdl	0.67	0.01	0.01	0.00	0.05	0.04	0.04	0.05	0.00	0.00	0.02	0.05	0.00	0.00	100.45
		B_1.06c	92.43	0.02	5.79	bdl	bdl	0.04	0.05	1.01	0.28	0.01	0.03	bdl	0.05	bdl	0.00	0.00	99.60
		B_1.06d	50.05	0.03	25.07	0.01	0.02	0.10	0.08	2.44	3.24	0.05	0.03	0.02	0.00	bdl	0.00	0.00	81.10
		B_1.10a	50.90	0.03	33.68	0.13	bdl	0.13	0.05	1.66	6.22	0.00	0.12	0.04	0.04	bdl	0.00	0.00	92.98
		B_1.11a	52.33	bdl	31.93	0.09	0.00	0.08	0.07	0.29	8.08	0.07	0.03	0.02	0.15	bdl	0.00	0.00	93.00
	B_1.15a	68.06	0.02	24.01	0.00	0.00	0.10	0.39	3.14	0.93	bdl	0.13	bdl	0.03	0.03	0.00	0.00	96.82	
	Rursee 2 BPV	B_2.02a	78.24	bdl	0.25	0.32	0.00	0.04	0.37	0.22	0.03	0.19	0.05	bdl	0.05	0.03	0.00	0.00	79.76
		B_2.02b	13.65	0.03	1.51	59.78	bdl	0.31	0.37	1.52	0.95	0.16	0.61	0.02	bdl	0.04	0.00	0.00	78.90
		B_2.03a	47.72	0.07	6.23	5.85	0.15	5.35	3.09	1.64	0.40	0.05	0.20	0.04	bdl	0.01	0.00	0.00	70.79
		B_2.03b	55.38	0.58	2.11	12.35	0.34	9.12	12.46	0.64	0.24	0.02	0.07	bdl	0.04	bdl	0.00	0.00	93.29
		B_2.03c	35.63	bdl	0.79	37.24	0.15	0.22	1.06	1.02	0.56	0.12	0.25	0.00	bdl	0.01	0.00	0.00	77.02
		B_2.04a	24.10	0.01	22.59	30.81	0.18	7.20	0.03	0.04	0.03	0.05	0.01	0.00	0.03	0.01	0.00	0.00	85.09
		B_2.05a	24.15	0.04	22.79	31.10	0.15	8.04	bdl	0.01	bdl	0.00	0.00	bdl	bdl	bdl	0.00	0.00	86.14
		B_2.09a	23.19	0.04	23.09	33.29	0.20	7.22	0.03	0.01	0.03	0.00	0.02	0.02	0.00	0.01	0.00	11.05	98.18
		B_2.09b	47.70	0.05	35.29	0.83	0.02	0.88	0.01	0.28	8.78	0.00	0.02	0.13	0.13	bdl	0.00	4.59	98.70
B_2.12a		100.15	bdl	0.06	1.62	0.00	0.01	0.02	0.01	0.00	0.06	0.02	bdl	bdl	bdl	0.00	0.00	101.78	
B_2.12b	56.62	bdl	1.83	26.39	0.02	0.04	0.05	0.13	0.33	0.55	0.32	0.07	0.00	0.00	0.00	0.00	86.34		
Rursee quartz veins	Rursee 2.1 BNV	B_2.1-03	97.91	0.02	0.04	1.69	0.00	0.01	0.00	0.01	0.00	0.00	0.02	bdl	0.00	bdl	0.00	0.00	99.58
		B_2.1-05a	100.31	bdl	0.32	0.19	0.02	0.02	0.00	0.02	0.01	0.00	bdl	bdl	bdl	0.00	0.00	100.80	
		B_2.1-07a	45.73	bdl	0.36	0.11	29.58	0.22	1.79	0.38	1.25	0.02	0.29	bdl	bdl	bdl	0.00	0.00	77.74
		B_2.1-07b	52.22	0.02	0.24	0.05	24.09	0.21	1.52	0.29	0.89	0.00	0.22	bdl	0.03	bdl	0.00	0.00	78.46
		B_2.1-07c	61.70	0.01	0.23	0.10	21.09	0.20	1.21	0.18	0.72	0.01	0.25	bdl	0.02	bdl	0.00	0.00	84.39
		B_2.1-11a	40.79	0.07	26.15	19.64	0.10	3.03	0.01	0.28	3.65	0.03	0.03	0.05	0.12	0.05	0.00	0.00	94.03
		B_2.1-11b	67.46	0.01	15.25	4.91	0.01	0.84	0.07	0.14	3.41	2.12	0.03	0.13	bdl	bdl	0.00	0.00	94.24
	Rursee 3 BPV	B_3.02a	42.77	0.01	15.84	22.60	0.17	4.89	0.07	0.02	0.67	0.07	0.15	bdl	bdl	bdl	0.00	0.00	87.12
		B_3.02b	66.75	0.02	9.82	13.59	0.08	3.14	bdl	0.05	0.17	0.02	0.03	0.00	0.04	0.02	0.00	0.00	93.70
		B_3.02c	90.77	0.02	3.20	3.97	0.03	1.03	bdl	bdl	0.04	0.01	0.00	0.00	0.00	0.05	0.00	0.00	99.08
		B_3.02d	24.66	0.01	21.55	27.73	0.16	6.22	0.06	0.04	0.79	0.53	0.21	0.07	bdl	0.00	0.00	0.00	81.96
		B_3.05a	30.48	0.03	23.88	25.27	0.16	7.25	0.03	0.03	0.29	0.04	0.06	bdl	bdl	bdl	0.00	0.00	87.44
		B_3.05b	39.46	0.00	30.20	13.10	0.06	2.88	0.05	0.16	2.88	0.18	0.10	0.08	bdl	0.09	0.00	0.00	89.24
		B_3.05c	64.23	0.03	16.31	2.75	0.00	1.11	0.01	0.11	4.01	0.01	0.06	bdl	bdl	bdl	0.00	0.00	88.58
B_3.08a	56.03	0.26	21.87	6.45	0.01	2.10	0.02	0.15	4.74	0.03	0.00	0.09	0.05	bdl	0.00	0.00	91.79		
B_3.08b	70.37	0.01	10.47	12.40	0.05	2.86	0.03	0.00	0.62	0.01	0.02	0.00	0.03	bdl	0.00	0.00	96.82		
B_3.08c	71.23	bdl	15.55	3.49	0.03	0.74	0.04	7.15	0.08	bdl	0.01	0.01	bdl	bdl	0.00	0.00	98.29		
B_3.08d	32.87	0.73	19.01	25.07	0.13	8.40	0.01	0.07	0.09	0.01	0.01	bdl	bdl	0.01	0.00	0.00	86.40		
B_3.11a	64.26	0.01	1.66	9.68	0.06	0.00	0.23	0.33	0.13	0.17	0.16	0.02	0.03	bdl	0.00	0.00	76.76		
B_3.11b	51.24	bdl	12.87	20.70	0.11	4.48	0.01	bdl	0.01	bdl	0.01	0.02	0.03	0.05	0.00	0.00	89.48		
Rursee 4 BPV	B_4.02a	47.91	0.07	3.98	1.07	0.01	0.22	0.58	2.30	2.47	0.15	0.34	0.10	0.06	bdl	0.00	0.00	59.23	
	B_4.03	100.84	0.00	bdl	0.02	0.00	0.00	0.02	0.00	0.02	bdl	0.02	bdl	0.08	bdl	0.00	0.00	100.78	
	B_4.04	32.13	0.05	3.95	22.69	0.00	0.15	6.00	0.63	0.64	0.17	0.27	0.13	bdl	0.01	0.00	0.00	66.80	
	B_4.05	85.80	0.00	0.03	0.01	0.02	0.02	0.32	0.02	0.03	0.24	0.03	bdl	0.71	bdl	0.00	0.00	87.15	
	B_4.08	78.34	0.01	0.73	0.04	10.49	0.22	0.96	0.07	0.09	0.00	0.06	bdl	bdl	bdl	0.00	0.00	90.27	
Rursee 5 BNV	B_5-03	60.18	0.12	1.28	1.08	0.05	1.33	3.01	0.98	0.97	0.11	0.37	0.00	bdl	bdl	0.00	0.00	69.38	
	B_5-05	96.03	0.12	0.42	0.22	0.03	0.02	0.08	0.07	0.11	0.04	0.01	bdl	0.00	0.00	0.00	0.00	97.09	
	B_5-06a	39.40	0.03	5.43	49.86	0.21	0.23	0.17	0.27	0.51	0.93	0.19	0.00	bdl	0.07	0.00	0.00	97.27	
	B_5-06b	48.32	0.09	36.38	0.65	0.00	0.66	0.03	0.45	9.16	0.01	0.01	0.10	0.15	bdl	0.00	0.00	95.97	
	B_5-06c	47.07	0.05	34.95	0.69	bdl	0.67	0.06	0.35	9.02	0.00	0.02	0.14	0.06	0.06	0.00	0.00	93.12	
	B_5-07	83.67	0.01	8.19	0.07	bdl	0.03	0.13	0.09	2.24	0.07	0.03	bdl	bdl	0.00	0.00	0.00	94.48	

Table 2. Continued.

EPMA analysis of mineral inclusions and microfractures of clean fraction of quartz veins' grain of Rursee samples (wt %).																					
	Sample ID	Grain ID	SiO ₂	TiO ₂	Al ₂ O ₃	FeO	MnO	MgO	CaO	Na ₂ O	K ₂ O	P ₂ O ₅	Cl	F	BaO	ZrO ₂	O	H ₂ O	TOTAL		
Rursee quartz veins	Rursee 6 BPV	B_6-07b	85.19	0.02	8.13	0.00	bdl	bdl	0.12	1.28	0.71	0.07	0.03	bdl	bdl	0.02	0.00	0.00	95.52		
		B_6-07a	79.39	0.00	3.32	0.00	0.01	0.03	0.31	0.06	0.94	0.24	0.09	bdl	bdl	bdl	0.00	0.00	84.32		
		B_6-16a	49.44	bdl	37.34	0.06	bdl	0.10	0.08	5.13	1.63	0.01	0.02	0.05	0.04	bdl	0.00	0.00	93.85		
		B_6-16b	57.16	0.01	19.71	0.03	bdl	0.06	0.16	2.85	1.57	0.03	0.03	bdl	0.05	bdl	0.00	0.00	81.61		
		B_6-17	30.47	0.03	21.91	31.64	0.17	6.42	0.01	0.02	0.02	0.02	bdl	bdl	bdl	0.00	0.00	90.55			
B_6-19	69.23	0.04	17.80	0.12	bdl	0.04	0.04	0.46	4.81	0.00	0.02	0.03	0.00	0.01	bdl	0.00	0.00	92.51			
Internal standard of UU	KL2-2		50.09	2.55	13.10	10.78	0.17	6.99	10.80	2.33	0.47	0.25	0.00	0.00	0.01	bdl	0.00	0.00	97.49		
			50.37	2.59	13.11	10.79	0.14	6.93	10.94	2.42	0.51	0.25	0.00	bdl	0.04	bdl	0.00	0.00	98.00		
			50.27	2.65	13.13	10.83	0.16	6.97	10.93	2.30	0.46	0.27	0.01	bdl	bdl	0.01	0.00	0.00	97.95		
Internal standard of UU	ATHO-2		74.10	0.23	12.11	3.37	0.10	0.11	1.63	3.60	2.80	0.03	0.05	0.04	0.04	0.02	0.00	0.00	98.23		
			74.00	0.24	12.22	3.38	0.10	0.09	1.59	3.60	2.68	0.03	0.04	0.10	0.06	0.01	0.00	0.00	98.13		
			74.39	0.21	12.11	3.41	0.10	0.09	1.63	3.55	2.70	0.06	0.04	0.02	0.08	0.08	0.00	0.00	98.48		
Internal standard of UU	KL2-3		51.64	2.60	13.46	10.89	0.19	7.46	10.98	2.33	0.47	0.30	0.00	bdl	0.00	0.02	0.00	0.00	100.29		
			50.51	2.62	13.24	10.82	0.13	7.29	10.81	2.28	0.48	0.29	0.00	bdl	bdl	0.04	0.00	0.00	98.43		
			50.83	2.61	13.13	10.97	0.15	7.29	11.01	2.30	0.48	0.29	0.01	bdl	bdl	0.02	0.00	0.00	99.00		
Internal standard of UU	ATHO-3		76.25	0.24	12.22	3.29	0.10	0.09	1.62	3.65	2.77	0.04	0.05	0.06	0.03	0.11	0.00	0.00	100.53		
			75.81	0.24	12.01	3.32	0.10	0.10	1.62	3.55	2.76	0.02	0.03	0.04	0.08	bdl	0.00	0.00	99.63		
			75.50	0.26	12.08	3.39	0.10	0.11	1.63	3.69	2.68	0.00	0.03	0.08	0.05	0.07	0.00	0.00	99.67		
EPMA analysis of crystal lattice of clean fraction of quartz veins' grain of Rursee samples (wt %).																					
	Veins' generation	Grain ID	SiO ₂	TiO ₂	Al ₂ O ₃	FeO	MnO	MgO	CaO	Na ₂ O	K ₂ O	P ₂ O ₅	Cl	F	BaO	ZrO ₂	O	H ₂ O	TOTAL		
Rursee quartz veins	Bedding-normal Veins	AH2_1_04	101.97	bdl	0.03	0.00	bdl	0.00	bdl	0.00	0.00	0.00	bdl	0.00	0.01	0.00	bdl	0.00	101.91		
		AH2_1_05	101.47	0.00	bdl	bdl	0.00	bdl	0.00	0.01	bdl	0.00	0.00	bdl	0.01	0.02	0.00	bdl	0.00	101.38	
		AH2_1_07	101.68	0.00	0.03	bdl	0.00	0.01	bdl	0.01	0.01	0.00	0.01	bdl	0.02	bdl	0.00	bdl	0.00	101.68	
	Bedding-parallel Veins	AH2_05	102.67	bdl	0.01	bdl	bdl	0.00	0.01	bdl	0.00	bdl	0.00	bdl	0.01	0.01	bdl	0.00	bdl	0.00	102.61
		AH2_06	102.41	0.02	0.08	bdl	bdl	bdl	0.00	0.02	0.01	0.00	0.00	bdl	0.06	bdl	0.00	bdl	0.00	102.48	
		AH2_07	101.69	bdl	0.05	0.00	bdl	0.01	bdl	bdl	bdl	0.01	0.00	bdl	0.00	0.02	0.00	bdl	0.00	101.61	
		AH2_08	101.42	0.01	0.03	0.01	0.00	bdl	0.00	bdl	0.00	bdl	0.01	0.01	bdl	bdl	0.07	0.00	bdl	0.00	101.47
		AH2_09	102.34	0.01	0.04	bdl	0.00	bdl	bdl	bdl	bdl	bdl	bdl	0.00	bdl	0.03	bdl	0.00	bdl	0.00	102.22

* bdl – below detection limit.

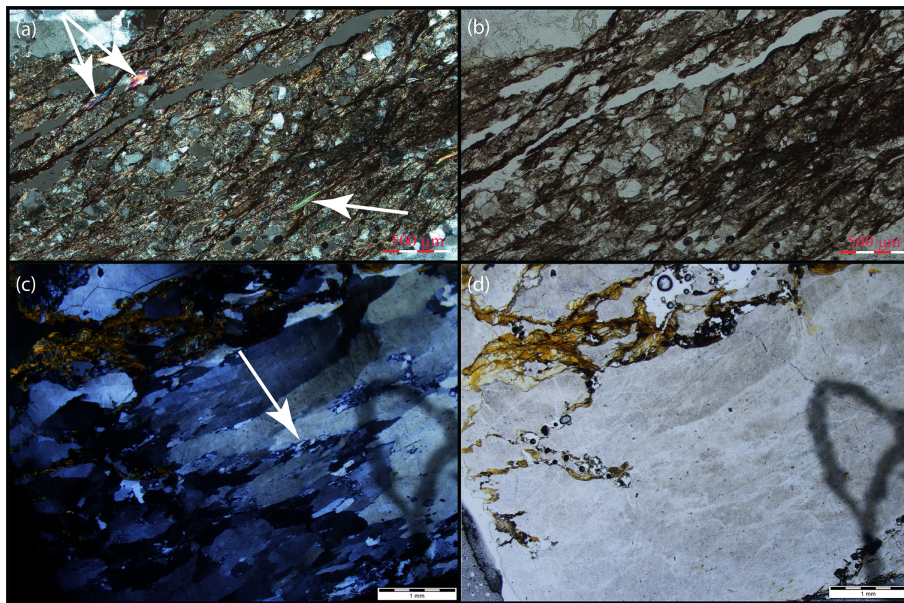


Figure 9. Microscopic image of the quartz vein host rock matrix from the Rursee formation. (a) Crossed polarizer and (b) plane polarizer images of the pelitic host rock (Rursee 2 BPV). White arrows (image a) indicate the presence of the white mica and sericite in the host pelitic rock. (c) Crossed polarizer and (d) plane polarizer images of the quartz veins' matrix (Rursee 1 BNV). The white arrow (image c) shows the presence of the quartz sub-grains. Quartz sub-grains in the vein are due to the local tectonic activity, indicating that this period corresponds to tectonic activity.

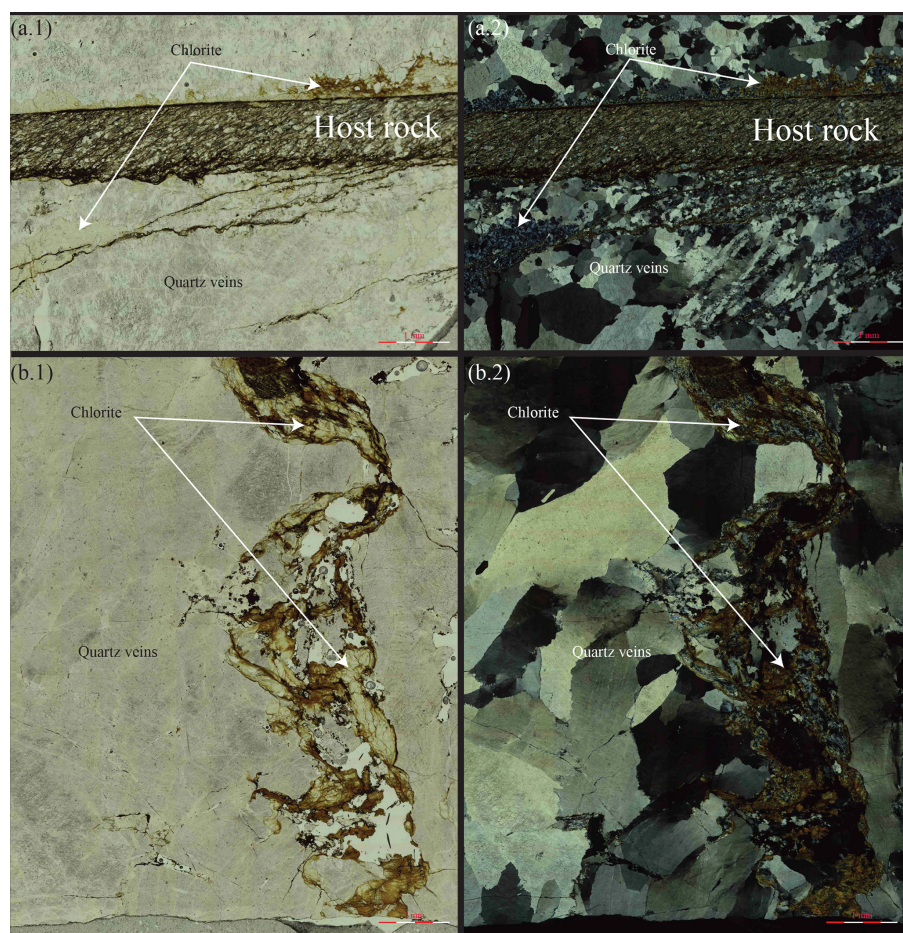


Figure 10. Chloritization distribution in the vein wall and fractures for both generations of quartz veins. **(a)** Plane **(a.1)** and crossed **(a.2)** polarizer of bedding-parallel veins: chloritization mainly between vein wall and host rock and fractures. **(b)** Plane **(b.1)** and crossed **(b.2)** polarizer of bedding-normal veins: chloritization in fractures.

al. (2024) demonstrated that a significant amount of fluid inclusion water can be extracted from these samples by a single crushing step using a spindle crusher. In this study, throughout the crushing process, the total amount of argon released steadily increases (Fig. 6). In the latter stages of the experiment (from the 20th analysing steps), the substantial release of $^{39}\text{Ar}_K$ isotopes may originate as follows:

- The gas release only from the small-sized fluid inclusions (i.e. $< 5\ \mu\text{m}$ pseudo-secondary) until the last stage of the experiment (~ 40 – 50 th analysing step) and then in the last stage (after the 50th step) from solid-phase K-bearing minerals and/or crystal lattice, which corresponds to the end of the early converging section in some samples. As $K/Cl > 1$ after (the 20th analysing step), the low peak ($\sim 1080\ \text{cm}^{-1}$) in Raman spectroscopy may correspond to a K-related component (e.g. K_2CO_3) from fluid inclusions.
- The significant release of $^{39}\text{Ar}_K$ isotopes in the middle to later stages of the experiment may be related

to the presence of non-crushed, small-sized fluid inclusions ($< 5\ \mu\text{m}$) together with K-bearing mineral inclusions in the samples and/or $^{40}\text{Ar}^*$ from the crystal lattice under the condition that the low peak in $\sim 1080\ \text{cm}^{-1}$ from Raman spectroscopy belongs to the epoxy background of the quartz grain. The contribution of crushing-induced degassing K-bearing mineral inclusions is also corroborated by EPMA data, and the presence of K in the lattice cannot be ruled out for the Rursee samples.

4.3 Age spectra and isochrons

As mentioned previously, the distribution of argon isotopes (Fig. 6) indicates that $^{39}\text{Ar}_K$ is derived from distinct sources, likely mineral inclusions and/or eventually crystal lattice rather than fluid inclusions in particular in the later phase of the experiment, which was used for the age determinations. These potential sources of K, including fluid and mineral inclusions and/or crystal lattice, may all contribute to

the variability observed in the age spectra derived from the different samples. Due to the presence of $^{40}\text{Ar}_E$ from the fluid inclusions, the initial analytical stages of the analyses yield anomalously high apparent ages in the first part of their age spectra (Fig. 4). Some samples (Rursee 3 BPV, Rursee 5 BNV, and Rursee 6 BPV) show an early converging section in the first part of the experiment. The early converging section effect occurs between the 20th and 30th analysing steps, which may be associated with sudden changes in K/Cl ratios (Fig. 7). These sudden changes may be due to the sharp transition from fluid-state reservoirs (e.g. small-sized fluid inclusions) to solid-state reservoirs (e.g. K-bearing mineral inclusions). However, it does not occur in the second group of quartz samples (Rursee 1b BNV, Rursee 2 BPV, Rursee 4 BPV), revealing smooth transitions from fluid to solid states of $^{39}\text{Ar}_K$ reservoirs. The transition for the Rursee 2.1 BNV is neither abrupt as for the first group samples nor smooth as for the second group samples; hence, the impact of the early converging section is minimal.

The transition from fluid-state reservoirs to solid-state reservoirs can be supported by grain size distribution (see Supplement file S4), indicating that fluid-state reservoirs may remain unreleased beyond around 800 crushes (around the 20th analysis step). However, the presence of small particles at the bottom of the crusher (non-recoverable size) after 800 crushes may result in the measured results not accurately representing the whole grain size distribution. As the grain size distribution depends on many factors (i.e. crushing efficiency, presence of microcracks), there may even be a factor of difference for two groups.

The impact of $^{40}\text{Ar}_E$ results in inverse isochrons (Fig. 5) during the initial stage. The relationship between the $^{36}\text{Ar}/^{40}\text{Ar}$ and $^{39}\text{Ar}/^{40}\text{Ar}$ for all samples resulted in a decrease in the $^{36}\text{Ar}/^{40}\text{Ar}$ ratio and an increase in the $^{39}\text{Ar}/^{40}\text{Ar}$ ratio (initial stage in Fig. 11). The presence of an elevated concentration of ^{36}Ar at the beginning of the experiment could be due to the atmospheric argon gas that is either trapped in the stainless steel crusher and/or the original fragment surfaces or perhaps released during the initial stage of crushing. Following the opening of fluid inclusions, the ratio of $^{36}\text{Ar}/^{40}\text{Ar}$ increases linearly with the ratio of $^{39}\text{Ar}/^{40}\text{Ar}$. This is probably due to a decrease in excess argon throughout the crushing and an increase in $^{39}\text{Ar}_K$ associated with K-bearing minerals and/or crystal lattice (intermediate stage in Fig. 11). In the last phase of $^{40}\text{Ar}/^{39}\text{Ar}$ analysis, the concentration of $^{39}\text{Ar}_K$ decreases (final stage in Fig. 11). This last part is particularly important for determining the age of quartz vein samples.

Inverse isochrons may assist in determining the maximum apparent age of fluid inclusions by linear regression of the data related to fluid inclusions. However, the high amounts of excess argon in the system obscure geologically meaningful ages.

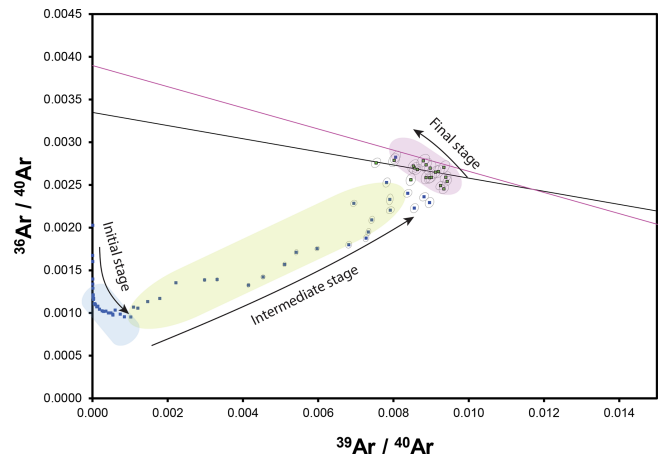


Figure 11. Inverse isochron representation of quartz veins (ex: Rursee 2.1 BNV): three stages: (1) initial stage with the opening of fluid inclusions, (2) intermediate stage where argon is released from mineral inclusions or microfractures and/or crystal lattice, and (3) final stage of argon release from mineral inclusions and neglectable excess argon in samples.

4.4 Implications

Unlike studies that obtained consistent maximum apparent ages from high-salinity (> 20 eq. wt % NaCl) primary fluid inclusions of garnet (in eclogite) and wolframite (Qiu and Wijbrans, 2006; Qiu et al., 2011; Bai et al., 2013, 2019), we were unable to date pseudo-secondary and secondary fluid inclusions in recrystallized Rursee quartz samples, likely due to high $^{40}\text{Ar}_E$ concentrations and/or low salinity (3.5–8 eq. wt % NaCl). The reduced K concentration in the pseudo-secondary and secondary fluid inclusions, due to the loss of the primary brine and its replacement by a lower-salinity, lower-K fluid, likely led to inaccurate maximum apparent age determination. While no precise age was determined for the fluid inclusions, $^{40}\text{Ar}/^{36}\text{Ar}$ ratios (above atmospheric but below 4000) indicate a mixed metamorphic–meteoric fluid source (Ballentine et al., 2002; Ozima and Podosek, 2002). Later, during the crushing experiment, the K-bearing mineral inclusions may provide geologically meaningful ages, although the argon closure temperatures in quartz remain uncertain. For reference, the closure temperature of smaller-size sericite grains ($\sim 20\ \mu\text{m}$) corresponds to temperatures ($\sim 300\text{--}350\ ^\circ\text{C}$) (Glasmacher et al., 2001; Watson and Cherniak, 2003), while the vitrinite reflectance from psammatic and pelitic layers indicates maximum burial temperatures ($220\ ^\circ\text{C}$) near the Carboniferous–Permian boundary, with gradual cooling thereafter (Littke et al., 2012).

Three $^{40}\text{Ar}/^{39}\text{Ar}$ maximum apparent ages ranging from 117 to 84 Ma differ from the interpretation based on structural analyses, which posit that veining occurred during the early Variscan Orogeny (Van Noten et al., 2007), possibly due to argon loss during cooling and/or recrystallization.

The obtained maximum apparent ages may be influenced to some extent by the presence of neo-crystallized quartz sub-grains, although their volume appears relatively small (Fig. 9c). However, since the maximum apparent ages primarily reflect solid-phase reservoirs (i.e. K-bearing mineral inclusions) rather than fluid-phase components, likely, K-bearing solid-phase reservoirs intergrow simultaneously with the recrystallization process.

Post-Variscan tectonic activity is known for the southern Rhenish Massif due to late- and post-orogenic fault movements and coeval reactivation of Variscan structures leading to the fluids' (re)activity (Herbst and Muller, 1969; Schwab, 1987; Korsch and Schäfer, 1991; Hein and Behr, 1994; Moe, 2000; Kirnbauer et al., 2012).

Given that reactivation of existing veins could have occurred without forming new fractures (Virgo et al., 2013), this reactivation is usually associated with the infiltration of high-salinity (> 20 eq. wt % NaCl) fluids in central Europe and the Rhenish Massif (Behr et al., 1987; Redecke, 1992; Hein and Behr, 1994; Germann and Friedrich, 1999; Heijlen et al., 2001; Kuèera et al., 2010).

This saline fluid activity is at odds with the low-salinity fluid inclusions (3.5–8 eq. wt % NaCl) in the Rursee quartz veins (Van Noten et al., 2011). However, they agree with low-salinity fluid inclusions in quartz veins of the Rhenish Massif, which are attributed to upward migration of Variscan fluid remnants during Jurassic–Cretaceous reactivation (Kirnbauer et al., 2012).

Near Rursee (Stavelot inlier), low-salinity (0.2–7.2 eq. wt % NaCl) and high-temperature fluid activity ($\sim 250^\circ\text{C}$) along the Variscan front reflects warm meteoric fluid circulation (Schroyen and Muchez, 2000). Such warm, low-salinity fluids may have also contributed to the chloritization of veins in the Rursee outcrops. We propose that tectonic activity and quartz vein reactivation–recrystallization could explain the observed $^{40}\text{Ar}/^{39}\text{Ar}$ maximum apparent ages, as low-salinity Variscan fluids perhaps moved along the reactivated fractures, forming new quartz minerals within the Variscan-related veins during Jurassic–Cretaceous tectonic activity (i.e. opening of North Atlantic).

5 Conclusions

- The analysis of argon isotope patterns and their interpretations (including K/Cl and inverse isochrons) indicates that the main reservoir $^{39}\text{Ar}_\text{K}$ for geologically meaningful ages originated from the K-bearing minerals (illite–sericite and possibly chlorite) in quartz vein microcracks and/or cavities of fluid inclusions and/or crystal lattice of quartz.

- The determination of a primary crystallization age, i.e. Variscan age, for the quartz veins, is not feasible, owing to the low amount of K in fluid inclusions and the high amount of excess argon within the FIAs, resulting in anomalously old apparent ages in the first ~ 20 crushing steps.
- The reduced K concentration, due to the loss of primary fluid from inclusions and replacement by a lower-salinity, lower K fluid, led to bias in the age determination of fluid inclusions. The obtained ages potentially correspond either to the presences of a secondary generation of low-salinity fluids or to the contribution of radiogenic argon reservoirs hosted in solid phases related to intergrowth mineral inclusions during the recrystallization of quartz veins.
- The maximum apparent ages obtained from the quartz samples span the Jurassic–Cretaceous period. The presence of neo-crystallized quartz sub-grains in the veins is due to the local tectonic activity, indicating that this period corresponds to the tectonic activity of the Rhenish Massif.

Appendix A

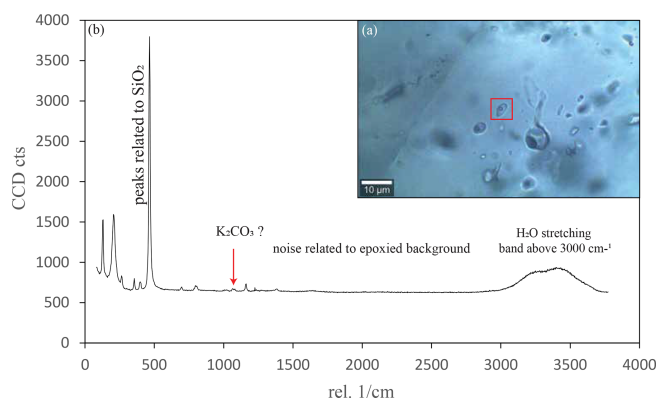


Figure A1. Raman spectroscopy of fluid inclusion from Rursee quartz veins. **(a)** Microscopic image of an epoxied and polished fluid-rich quartz fraction. The fluid inclusion that underwent Raman analysis is represented by the red box. **(b)** The Raman plot is presented with the wavelength on the x axis and intensity on the y axis. The Raman spectra show a stretching band in the wavelength range of 3000 to 3700 cm^{-1} , which indicates the presence of an aqueous system.

Appendix B

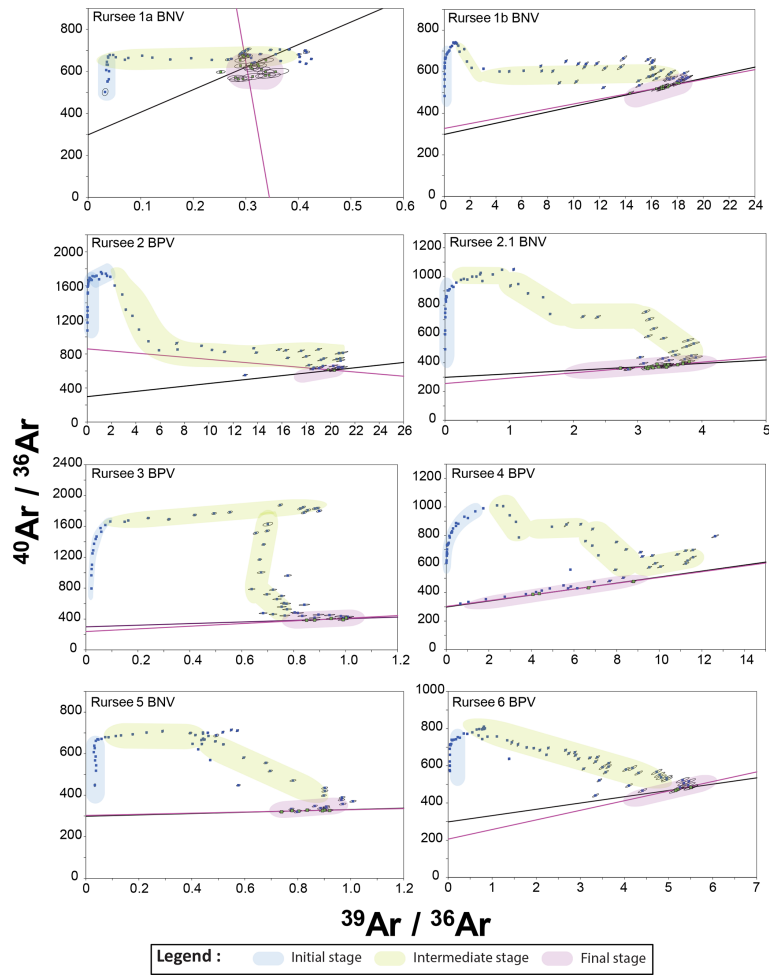


Figure B1. Normal isochron plots of all quartz vein samples.

Appendix C

Table C1. Rursee quartz vein samples' J values and mass-dependent fractionation (MDF) with analytical error.

Sample ID	Sample ID Ar	MDF	1σ %	J value	1σ %
Rursee 1a BNV	R01a	0.99635	± 0.04	0.0034347	± 0.06
Rursee 1b BNV	R01b	0.99519	± 0.04	0.0034737	± 0.06
Rursee 2 BPV	R02	0.99469	± 0.03	0.0035113	± 0.03
Rursee 2.1 BNV	R021	0.99492	± 0.03	0.0034868	± 0.04
Rursee 3 BPV	R03	0.99868	± 0.03	0.0035113	± 0.03
Rursee 4 BPV	R04	0.99749	± 0.03	0.0035113	± 0.03
Rursee 5 BNV	R05	0.99494	± 0.04	0.0034868	± 0.04
Rursee 6 BPV	R06	0.99709	± 0.04	0.0034868	± 0.04

Data availability. All data are included in the tables, appendices, and the Supplement.

Supplement. The supplement related to this article is available online at <https://doi.org/10.5194/gchron-7-173-2025-supplement>.

Author contributions. The paper was primarily authored by AAOH, who is the corresponding author. Co-authors KK, JW, and JvdL made substantial contributions to data interpretation and refinement of the paper, enhancing its clarity and depth.

Competing interests. The contact author has declared that none of the authors has any competing interests.

Disclaimer. Publisher's note: Copernicus Publications remains neutral with regard to jurisdictional claims made in the text, published maps, institutional affiliations, or any other geographical representation in this paper. While Copernicus Publications makes every effort to include appropriate place names, the final responsibility lies with the authors.

Acknowledgements. This study has been funded by the FluidNET Consortium of the EU H2020 Marie Skłodowska-Curie Action (no. 956127). We would like to thank Stefan Groen for his assistance in data management and the $^{40}\text{Ar}/^{39}\text{Ar}$ analysis laboratory, as well as Roel van Elsas for his help in the Mineral Separation Laboratory at VU Amsterdam. We are grateful to Bouke Lacet for preparing the epoxy grain mounts and thin sections and to Eric Hellebrand and Tilly Bouten for the EPMA analysis. Finally, this study would have been impossible without the support of Janos L. Urai, who introduced us to the Rursee outcrops and unfortunately passed away. We sincerely thank the reviewers, Alexei Ivanov and Hua-Ning Qiu, for their insightful and constructive feedback, which significantly improved the quality of this article.

Financial support. This research has been supported by the FluidNET Consortium of the EU H2020 Marie Skłodowska-Curie Action (grant no. 956127).

Review statement. This paper was edited by Fred Jourdan and reviewed by Alexei Ivanov and Hua-Ning Qiu.

References

Bähr, R.: Das U Th/He-System in Hämatit als Chronometer für Mineralisationen, PhD Thesis, University of Heidelberg, Vol. 245, 1–244, <https://www.osti.gov/etdweb/biblio/7007711> (last access: 12 May 2025), 1987.

- Bai, X. J., Wang, M., Jiang, Y. D., and Qiu, H.-N.: Direct dating of tin–tungsten mineralization of the Piaotang tungsten deposit, South China, by $^{40}\text{Ar}/^{39}\text{Ar}$ progressive crushing, *Geochim. Cosmochim. Ac.*, 114, 1–12, 2013.
- Bai, X. J., Hu, R.-G., Jiang, Y.-D., Liu, X., Tang, B., and Qiu, H.-N.: Refined insight into $^{40}\text{Ar}/^{39}\text{Ar}$ progressive crushing technique from K–Cl–Ar correlations in fluid inclusions, *Chem. Geol.*, 515, 37–49, <https://doi.org/10.1016/j.chemgeo.2019.03.037>, 2019.
- Bai, X. J., Liu, M., Hu, R. G., Fang, Y., Liu, X., Tang, B., and Qiu, H. N.: Well-Constrained Mineralization Ages by Integrated $^{40}\text{Ar}/^{39}\text{Ar}$ and U–Pb Dating Techniques for the Xitian W–Sn Polymetallic Deposit, South China, *Econ. Geol.*, 117, 833–852, <https://doi.org/10.5382/econgeo.4889>, 2022.
- Baksi, A. K.: Geochronological studies on whole-rock basalts, Deccan Traps, India: Evaluation of the timing of volcanism relative to the K–T boundary, *Earth Planet. Sc. Lett.*, 121, 43–56, [https://doi.org/10.1016/0012-821X\(94\)90030-2](https://doi.org/10.1016/0012-821X(94)90030-2), 1994.
- Baksi, A. K.: A quantitative tool for detecting alteration in undisturbed rocks and minerals – II: Application to argon ages related to hotspots, in: Foulger, G. R. and Jurdy, D. M., *Plates, Plumes and Planetary Processes Geological Society of America*, [https://doi.org/10.1130/2007.2430\(16\)](https://doi.org/10.1130/2007.2430(16)), 2007.
- Ballentine, C. J., Burgess, R., and Marty, B.: Tracing fluid origin, transport and interaction in the crust, <https://repository.geologyscience.ru/handle/123456789/29036> (last access: 14 December 2023), 2002.
- Bambauer, H. U.: Spurenelementgehalte und g-Farbzentren in Quarzen aus Zerrklüften der Schweizer Alpen, *Schweiz. Miner. Petrol.*, 41, 335–369, 1961.
- Baumgartner, L. P. and Ferry, J. M.: A model for coupled fluid-flow and mixed-volatile mineral reactions with applications to regional metamorphism, *Contrib. Mineral. Petr.*, 106, 273–285, 1991.
- Behr, H.-J., Horn, E. E., Frenzel-Beyme, K., and Reutel, Chr.: Fluid inclusion characteristics of the Variscan and post-Variscan mineralizing fluids in the Federal Republic of Germany, *Chem. Geol.*, 61, 273–285, [https://doi.org/10.1016/0009-2541\(87\)90046-5](https://doi.org/10.1016/0009-2541(87)90046-5), 1987.
- Bonhomme, M. G., Bühmann, D., and Besnus, Y.: Reliability of K–Ar Dating of Clays and Silicifications Associated with vein Mineralizations in Western Europe, *Geol. Rundsch.*, 72, 105–117, <https://doi.org/10.1007/BF01765902>, 1983.
- Burnard, P., Graham, D., and Turner, G.: Vesicle-Specific Noble Gas Analyses of “Popping Rock”: Implications for Primordial Noble Gases in Earth, *Science*, 276, 568–571, <https://doi.org/10.1126/science.276.5312.568>, 1997.
- Cartwright, I. and Buick, I. S.: Fluid generation, vein formation and the degree of fluid–rock interaction during decompression of high-pressure terranes: The Schistes Lustres, Alpine Corsica, France, *J. Metamorph. Geol.*, 18, 607–624, <https://doi.org/10.1046/j.1525-1314.2000.00280.x>, 2000.
- Cartwright, J. A., Gilmour, J. D., and Burgess, R.: Martian fluid and Martian weathering signatures identified in Nakhla, NWA 998 and MIL 03346 by halogen and noble gas analysis, *Geochim. Cosmochim. Ac.*, 105, 255–293, 2013.
- Chatziliadou, M. and Kramm, U.: Rb–Sr Alter und Sr–Pb Isotopencharakteristik von Gangmineralisationen in paläozoischen Gesteinen am Nordrand des linksrheinischen Schiefergebirges (Raum Stolberg–Aachen–Kelmis) und Vergleich mit

- den rezenten Thermalwässern von Aachen-Burtscheid (RWTH-CONV-113503, Publikationsserver der RWTH Aachen University), <https://publications.rwth-aachen.de/record/51191> (last access: 23 April 2024), 2009.
- Cox, S. F.: Structural and isotopic constraints on fluid flow regimes and fluid pathways during upper crustal deformation: An example from the Taemas area of the Lachlan Orogen, SE Australia, *J. Geophys. Res.-Sol. Ea.*, 112, B08208, <https://doi.org/10.1029/2006JB004734>, 2007.
- Féraud, G. and Courtillot, V.: Comment on: “Did Deccan volcanism pre-date the Cretaceous-Tertiary transition?”, *Earth Planet. Sc. Lett.*, 122, 259–262, [https://doi.org/10.1016/0012-821X\(94\)90068-X](https://doi.org/10.1016/0012-821X(94)90068-X), 1994.
- Fielitz, W.: Variscan transpressive inversion in the north-western central Rhenohercynian belt of western Germany, *J. Struct. Geol.*, 14, 547–563, [https://doi.org/10.1016/0191-8141\(92\)90156-Q](https://doi.org/10.1016/0191-8141(92)90156-Q), 1992.
- Fielitz, W.: Epizonal to lower mesozonal diastathermal metamorphism in the Ardennes (Rhenohercynian belt of western central Europe), *Terra Nostra*, 95, p. 95, 1995.
- Foland, K. A.: $^{40}\text{Ar}/^{39}\text{Ar}$ incremental heating plateaus for biotites with excess argon, *Chem. Geol.*, 41, 3–21, [https://doi.org/10.1016/S0009-2541\(83\)80002-3](https://doi.org/10.1016/S0009-2541(83)80002-3), 1983.
- Franzke, H. J. and Anderle, H.-J.: Metallogenesis, in: Dallmeyer, R. D., Franke, W., and Weber, K., *Pre-Permian Geology of Central and Eastern Europe*, Springer, 138–150, https://doi.org/10.1007/978-3-642-77518-5_13, 1995.
- Germann, A. and Friedrich, G.: Strukturkontrollierte, post-variskische Buntmetallmineralisation in paläozoischen und mesozoischen Sedimentgesteinen der nordwestlichen Eifel, *Zeitschrift Der Deutschen Geologischen Gesellschaft*, 513–541, 1999.
- Glasmacher, U., Zentilli, M., and Grist, A. M.: Apatite Fission Track Thermochronology of Paleozoic Sandstones and the Hill-Intrusion, Northern Linksrheinisches Schiefergebirge, Germany. *Advances in Fission-Track Geochronology*, Springer Netherlands, 151–172, https://doi.org/10.1007/978-94-015-9133-1_10, 1998.
- Glasmacher, U., Tschernoster, R., Clauer, N., and Spaeth, G.: K–Ar dating of magmatic sericite crystallites for determination of cooling paths of metamorphic overprints, *Chem. Geol.*, 175, 673–687, [https://doi.org/10.1016/S0009-2541\(00\)00292-8](https://doi.org/10.1016/S0009-2541(00)00292-8), 2001.
- Goemaere, E. and Dejonghe, L.: Paleoenvironmental reconstruction of the Mirwart Formation (Pragian) in the Lambert Quarry (Flamierge, Belgium), *Geol. Belg.*, 8, 3–14, 2005.
- Götze, J., Pan, Y., and Müller, A.: Mineralogy and mineral chemistry of quartz: A review, *Mineral. Mag.*, 85, 639–664, <https://doi.org/10.1180/mgm.2021.72>, 2021.
- Heijlen, W., Muchez, P., and Banks, D. A.: Origin and evolution of high-salinity, Zn–Pb mineralising fluids in the Variscides of Belgium, *Miner. Deposita*, 36, 165–176, <https://doi.org/10.1007/s001260050296>, 2001.
- Hein, U. F. and Behr, H. J.: Zur Entwicklung von Fluidsystemen im Verlauf der Deformationsgeschichte des Rhenohercynikums, *Go'ttinger Arbeiten zur Geologie und Paläontologie*, Sonderband 1, 191–193, 1994.
- Herbst, F. and Muller, H.-G.: Raum und Bedeutung des Emser Gangzuges, *Gewerkschaft Mercur*, 1969.
- Huseynov, A. A. O., van der Lubbe (Jeroen), H. J. L., Verdegaaal-Warmerdam, S. J. A., Postma, O., Schröder, J., and Vonhof, H.: Novel Crushing Technique for Measuring $\delta^{18}\text{O}$ and $\delta^2\text{H}$ Values of Fluid Inclusions (H_2O) in Quartz Mineral Veins Using Cavity Ring-Down Spectroscopy, *Geofluids*, 2024, 5795441, <https://doi.org/10.1155/2024/5795441>, 2024.
- IJlst, L.: A laboratory overflow-centrifuge for heavy liquid mineral separation, *Am. Mineral.*, 58, 1088–1093, 1973.
- Jakobus, R.: Die Erzgänge des östlichen Taunus, *Geol. Jahrb. Hess.*, 120, 145–160, 1992.
- Jiang, Y. D., Qiu, H.-N., and Xu, Y. G.: Hydrothermal fluids, argon isotopes and mineralization ages of the Fankou Pb–Zn deposit in south China: Insights from sphalerite $^{40}\text{Ar}/^{39}\text{Ar}$ progressive crushing, *Geochim. Cosmochim. Ac.*, 84, 369–379, 2012.
- Jourdan, A.-L., Vennemann, T. W., Mullis, J., and Ramseier, K.: Oxygen isotope sector zoning in natural hydrothermal quartz, *Mineral. Mag.*, 73, 615–632, <https://doi.org/10.1180/minmag.2009.073.4.615>, 2009.
- Kats, A.: Hydrogen in alpha-quartz, *Philips Res. Rep.*, 17, 133–195, 1962.
- Kelley, S., Turner, G., Butterfield, A. W., and Shepherd, T. J.: The source and significance of argon isotopes in fluid inclusions from areas of mineralization, *Earth Planet. Sc. Lett.*, 79, 303–318, 1986.
- Kendrick, M. A.: Comment on “Paleozoic ages and excess ^{40}Ar in garnets from the Bixiling eclogite in Dabieshan, China: New insights from $^{40}\text{Ar}/^{39}\text{Ar}$ dating by stepwise crushing by Hua-Ning Qiu and J.R. Wijbrans”, *Geochim. Cosmochim. Ac.*, 71, 6040–6045, <https://doi.org/10.1016/j.gca.2007.01.029>, 2007.
- Kendrick, M. A. and Phillips, D.: Discussion of “the Paleozoic metamorphic history of the Central Orogenic Belt of China from $^{40}\text{Ar}/^{39}\text{Ar}$ geochronology of eclogite garnet fluid inclusions by Qiu Hua-Ning and Wijbrans J. R.”, *Earth Planet. Sc. Lett.*, 279, 392–394, <https://doi.org/10.1016/j.epsl.2008.12.047>, 2009.
- Kendrick, M. A., Burgess, R., Patrick, R. A. D., and Turner, P. G.: Halogen and Ar–Ar age determinations of inclusions within quartz veins from porphyry copper deposits using complementary noble gas extraction techniques, *Chem. Geol.*, 177, 351–370, 2001.
- Kendrick, M. A., Miller, J. M., and Phillips, D.: Part II. Evaluation of ^{40}Ar – ^{39}Ar quartz ages: Implications for fluid inclusion retentivity and determination of initial $^{40}\text{Ar}/^{36}\text{Ar}$ values in Proterozoic samples, *Geochim. Cosmochim. Ac.*, 70, 2562–2576, 2006.
- Kendrick, M. A., Scambelluri, M., Honda, M., and Phillips, D.: High abundances of noble gas and chlorine delivered to the mantle by serpentinite subduction, *Nat. Geosci.*, 4, 807–812, <https://doi.org/10.1038/ngeo1270>, 2011.
- Kirnbauer, T., Wagner, T., Taubald, H., and Bode, M.: Post-Variscan hydrothermal vein mineralization, Taunus, Rhenish Massif (Germany): Constraints from stable and radiogenic isotope data, *Ore Geol. Rev.*, 48, 239–257, <https://doi.org/10.1016/j.oregeorev.2012.03.010>, 2012.
- Klügel, T.: Geometrie und Kinematik einer variszischen Plattengrenze. Der Südrand des Rhenohercynikums im Taunus, *Geol. Abh. Hess.*, 101, 1–215, 1997.
- Kötonik, K., Piszczowska, A., Paszkowski, M., Sláma, J., Becker, R. T., Szczerba, M., Krawczyński, W., Hartenfels, S., and Marynowski, L.: Baltic provenance of top-Famennian siliciclastic material of the northern Rhenish Massif, Rhenohercynian

- zone of the Variscan orogen, *Int. J. Earth Sci.*, 107, 2645–2669, <https://doi.org/10.1007/s00531-018-1628-4>, 2018.
- Koppers, A. A. P.: ArArCALC – software for $^{40}\text{Ar}/^{39}\text{Ar}$ age calculations, *Comput. Geosci.*, 28, 605–619, [https://doi.org/10.1016/S0098-3004\(01\)00095-4](https://doi.org/10.1016/S0098-3004(01)00095-4), 2002.
- Korsch, R. J. and Schäfer, A.: Geological interpretation of DEKORP deep seismic reflection profiles 1C and 9N across the variscan Saar-Nahe Basin southwest Germany, *Tectonophysics*, 191, 127–146, [https://doi.org/10.1016/0040-1951\(91\)90236-L](https://doi.org/10.1016/0040-1951(91)90236-L), 1991
- Kučera, J., Muchez, P., Slobodník, M., and Prochaska, W.: Geochemistry of highly saline fluids in siliciclastic sequences: Genetic implications for post-Variscan fluid flow in the Moravosilesian Palaeozoic of the Czech Republic, *Int. J. Earth Sci.*, 99, 269–284, <https://doi.org/10.1007/s00531-008-0387-z>, 2010.
- Kuiper, K. F., Deino, A., Hilgen, F. J., Krijgsman, W., Renne, P. R., and Wijbrans, J. R.: Synchronizing Rock Clocks of Earth History, *Science*, 320, 500–504, <https://doi.org/10.1126/science.1154339>, 2008.
- Lee, J.-Y., Marti, K., Severinghaus, J. P., Kawamura, K., Yoo, H.-S., Lee, J. B., and Kim, J. S.: A redetermination of the isotopic abundances of atmospheric Ar, *Geochim. Cosmochim. Ac.*, 70, 4507–4512, <https://doi.org/10.1016/j.gca.2006.06.1563>, 2006.
- Li, C., Shen, P., Li, P., Sun, J., Feng, H., and Pan, H.: Changes in the factors controlling the chlorite composition and their influence on hydrothermal deposit studies: A case study from Hongguleleng Manto-type Cu deposit, *J. Geochem. Explor.*, 243, 107096, <https://doi.org/10.1016/j.gexplo.2022.107096>, 2022.
- Litke, R., Urai, J. L., Uffmann, A. K., and Risvanis, F.: Reflectance of dispersed vitrinite in Palaeozoic rocks with and without cleavage: Implications for burial and thermal history modeling in the Devonian of Rursee area, northern Rhenish Massif, Germany, *Int. J. Coal Geol.*, 89, 41–50, <https://doi.org/10.1016/j.coal.2011.07.006>, 2012.
- Liu, J., Wu, G., Qiu, H. N., and Li, Y.: $^{40}\text{Ar}/^{39}\text{Ar}$ dating, fluid inclusions and S-Pb isotope systematics of the Shabaosi gold deposit, Heilongjiang Province, China. *Geol. J.*, 50, 592–606, 2015.
- Lo, C.-H. and Onstott, T. C.: ^{39}Ar recoil artifacts in chloritized biotite, *Geochim. Cosmochim. Ac.*, 53, 2697–2711, [https://doi.org/10.1016/0016-7037\(89\)90141-5](https://doi.org/10.1016/0016-7037(89)90141-5), 1989.
- Lünenschloss, B., Muchez, P., and Bayer, U.: Late-Variscan fluid migration at the Variscan thrust front of Eastern Belgium: Numerical modelling of the palaeothermal and fluid flow field, *Int. J. Earth Sci.*, 97, 1201–1212, <https://doi.org/10.1007/s00531-007-0223-x>, 2008.
- Mansy, J. L., Everaerts, M., and De Vos, W.: Structural analysis of the adjacent Acadian and Variscan fold belts in Belgium and northern France from geophysical and geological evidence, *Tectonophysics*, 309, 99–116, [https://doi.org/10.1016/S0040-1951\(99\)00134-1](https://doi.org/10.1016/S0040-1951(99)00134-1), 1999.
- McKee, E. H., Conrad, J. E., Turrin, B. D., and Theodore, T. G.: $^{40}\text{Ar}/^{39}\text{Ar}$ studies of fluid inclusions in vein quartz from Battle Mountain, Nevada, *US Geological Survey Bulletin*, 2039, 155–165, https://books.google.de/books?hl=en&lr=&id=BVHIuwfhcpYC&oi=fnd&pg=PA155&dq=McKee,+E.+H.,+Conrad,+J.+E.,+Turrin,+B.+D.,+and+Theodore,+T.+G.:+50+40Ar+=+39Ar+studies+of+fluid+inclusions+in+vein+quartz+from+Battle+Mountain,+Nevada,+US+Geological+Survey+Bulletin,+2039,+155%E2%80%93+165TS6,+1993.&ots=ITb9Op0OyK&sig=GFYqiLylGNHImKEOWCZxbCc_iGA&redir_esc=y#v=onepage&q&f=false (last access: 30 November 2023), 1993.
- Mertz, D. F., Lippolt, H. J., and Müller, G.: Isotopengeochemische (K–Ar, $^{40}\text{Ar}/^{39}\text{Ar}$, Rb–Sr, $^{87}\text{Sr}/^{86}\text{Sr}$) und mineralogische Untersuchungen zur zeitlichen und genetischen Stellung postvariscischer Mineralisationen im Raum Saar-Nahe-Pfalz, *Fortschr. Mineral.*, 64, 116, 1986.
- Min, K., Mundil, R., Renne, P. R., and Ludwig, K. R.: A test for systematic errors in $^{40}\text{Ar}/^{39}\text{Ar}$ geochronology through comparison with U/Pb analysis of a 1.1-Ga rhyolite, *Geochim. Cosmochim. Ac.*, 64, 73–98, [https://doi.org/10.1016/S0016-7037\(99\)00204-5](https://doi.org/10.1016/S0016-7037(99)00204-5), 2000.
- Moe, A.: Structural development of a volcanic sequence of the Lahn area during the Variscan orogeny in the Rhenohercynian Belt (Germany), Dissertation, Heidelberg University, <https://doi.org/10.11588/heidok.00001095>, 2000.
- Muchez, P., Sintubin, M., and Swennen, R.: Origin and migration pattern of palaeofluids during orogeny: Discussion on the Variscides of Belgium and northern France, *J. Geochem. Explor.*, 69–70, 47–51, [https://doi.org/10.1016/S0375-6742\(00\)00008-X](https://doi.org/10.1016/S0375-6742(00)00008-X), 2000.
- Mullis, J., Dubessy, J., Poty, B., and O’Neil, J.: Fluid regimes during late stages of a continental collision: Physical, chemical, and stable isotope measurements of fluid inclusions in fissure quartz from a geotraverse through the Central Alps, Switzerland, *Geochim. Cosmochim. Ac.*, 58, 2239–2267, [https://doi.org/10.1016/0016-7037\(94\)90008-6](https://doi.org/10.1016/0016-7037(94)90008-6), 1994.
- Oliver, N. H. S. and Bons, P. D.: Mechanisms of fluid flow and fluid–rock interaction in fossil metamorphic hydrothermal systems inferred from vein–wallrock patterns, geometry and microstructure, *Geofluids*, 1, 137–162, <https://doi.org/10.1046/j.1468-8123.2001.00013.x>, 2001.
- Oncken, O., Von Winterfeld, C., and Dittmar, U.: Accretion of a rifted passive margin: The Late Paleozoic Rhenohercynian fold and thrust belt (Middle European Variscides), *Tectonics*, 18, 75–91, 1999.
- Onstott, T. C., Miller, M. L., Ewing, R. C., Arnold, G. W., and Walsh, D. S.: Recoil refinements: Implications for the $^{40}\text{Ar}/^{39}\text{Ar}$ dating technique, *Geochim. Cosmochim. Ac.*, 59, 1821–1834, [https://doi.org/10.1016/0016-7037\(95\)00085-E](https://doi.org/10.1016/0016-7037(95)00085-E), 1995.
- Ozima, M. and Podosek, F. A.: Noble gas geochemistry, Cambridge University Press, https://books.google.de/books?hl=en&lr=&id=TMIAfSle428C&oi=fnd&pg=PP1&dq=Ozima+2002&ots=nf7xTAXMps&sig=eqSMMUxvP69-FZOW2nMB91wYi61&redir_esc=y#v=onepage&q=Ozima2002&f=false (last access: 14 December 2024), 2002.
- Pacey, A., Wilkinson, J. J., and Cooke, D. R.: Chlorite and Epidote Mineral Chemistry in Porphyry Ore Systems: A Case Study of the Northparkes District, New South Wales, Australia, *Econ. Geol.*, 115, 701–727, <https://doi.org/10.5382/econgeo.4700>, 2020.
- Perny, B., Eberhardt, P., Ramseyer, K., Mullis, J., and Pankrath, R.: Microdistribution of Al, Li, and Na in á quartz: Possible causes and correlation with short-lived cathodoluminescence, *Am. Mineral.*, 77(5–6), 534–544, 1992.
- Porat, N.: Use of magnetic separation for purifying quartz for luminescence dating, *Ancient TL*, 24, 33–36, 2006.

- Potrafke, A., Stalder, R., Schmidt, B. C., and Ludwig, T.: OH defect contents in quartz in a granitic system at 1–5 kbar, *Contrib. Mineral. Petr.*, 174, 98, <https://doi.org/10.1007/s00410-019-1632-0>, 2019.
- Qiu, H.-N.: ^{40}Ar – ^{39}Ar dating of the quartz samples from two mineral deposits in western Yunnan (SW China) by crushing in vacuum, *Chem. Geol.*, 127, 211–222, 1996.
- Qiu, H.-N. and Dai, T. M.: $^{40}\text{Ar}/^{39}\text{Ar}$ techniques for dating the fluid inclusions of quartz from a hydrothermal deposit, *Chinese Sci. Bull.*, 34, 1887–1890, 1989.
- Qiu, H.-N. and Jiang, Y. D.: Sphalerite $^{40}\text{Ar}/^{39}\text{Ar}$ progressive crushing and stepwise heating techniques, *Earth Planet. Sc. Lett.*, 256, 224–232, 2007.
- Qiu, H.-N. and Wijbrans, J. R.: Paleozoic ages and excess ^{40}Ar in garnets from the Bixiling eclogite in Dabieshan, China: New insights from $^{40}\text{Ar}/^{39}\text{Ar}$ dating by stepwise crushing, *Geochim. Cosmochim. Ac.*, 70, 2354–2370, 2006.
- Qiu, H.-N. and Wijbrans, J. R.: The Paleozoic metamorphic history of the Central Orogenic Belt of China from $^{40}\text{Ar}/^{39}\text{Ar}$ geochronology of eclogite garnet fluid inclusions, *Earth Planet. Sc. Lett.*, 268, 501–514, <https://doi.org/10.1016/j.epsl.2008.01.042>, 2008.
- Qiu, H.-N. and Wijbrans, J. R.: Reply to comment by M. A. Kendrick and D. Phillips (2009) on “The Paleozoic metamorphic history of the Central Orogenic Belt of China from $^{40}\text{Ar}/^{39}\text{Ar}$ geochronology of eclogite garnet fluid inclusions” by Huang Ning Qiu and J. R. Wijbrans (2008) [*Earth Planet. Sc. Lett.* 268 (2008) 501–514], *Earth Planet. Sc. Lett.*, 279, 395–397, <https://doi.org/10.1016/j.epsl.2009.01.012>, 2009.
- Qiu, H.-N., Zhu, B., and Sun, D.: Age significance interpreted from ^{40}Ar – ^{39}Ar dating of quartz samples from the Dongchuan copper deposits, Yunnan, SW China, by crushing and heating, *Geochem. J.*, 36, 475–491, 2002.
- Qiu, H.-N., Wu, H. Y., Yun, J. B., Feng, Z. H., Xu, Y. G., Mei, L. F., and Wijbrans, J. R.: High-precision $^{40}\text{Ar}/^{39}\text{Ar}$ age of the gas emplacement into the Songliao Basin, *Geology*, 39, 451–454, <https://doi.org/10.1130/G31885.1>, 2011.
- Rama, S. N. I., Hart, S. R., and Roedder, E.: Excess radiogenic argon in fluid inclusions, *J. Geophys. Res.*, 70, 509–511, 1965.
- Ramsay, J. G.: The techniques of modern structural geology. *The Techniques of Modern Structural Geology, Folds and Fractures*, 2, 309–700, 1986.
- Rauchenstein-Martinek, K., Wagner, T., Wälle, M., and Heinrich, C. A.: Gold concentrations in metamorphic fluids: A LA-ICPMS study of fluid inclusions from the Alpine orogenic belt, *Chem. Geol.*, 385, 70–83, <https://doi.org/10.1016/j.chemgeo.2014.07.018>, 2014.
- Redecke, P.: Zur Geochemie und Genese variszischer und post-variszischer Buntmetallmineralisation in der Nordeifel und der Niederrheinischen Bucht, IML, 1992.
- Ribbert, K.-H., Brunemann, H.-G., Jäger, B., Knapp, G., Michel, G., M. Reinhaardt, M., Weber, M., and V. Wrede, V.: Geologische Karte von Nordrhein-Westfalen 1 : 100 000: Erläuterungen zu Blatt C5502 Aachen, Geologisches Landesamt Nordrhein-Westfalen, 1992.
- Schneider, J. and Haack, U.: Rb / Sr dating of silicified wall rocks of a giant hydrothermal quartz vein in the SE Rhenish Massif, Germany, *Mineral deposits: research and exploration. Where do they meet*, 971–972, 1997.
- Schneider, J., Haack, U., Hein, U. F., and Germann, A.: Direct Rb / Sr dating of sandstone-hosted sphalerites from stratabound Pb-Zn deposits in the northern Eifel, NW Rhenish Massif, Germany, in: *Mineral Deposits: Processes to Processing. Proceedings of the 5th Biennial. SGA Meeting and the 10th Quadrennial IAGOD Symposium*, edited by: Stanley, C. J., London, 22–25 August, 1287–1290, 1999.
- Schroyen, K. and Muchez, Ph.: Evolution of metamorphic fluids at the Variscan fold-and-thrust belt in eastern Belgium, *Sediment. Geol.*, 131, 3, [https://doi.org/10.1016/S0037-0738\(99\)00133-5](https://doi.org/10.1016/S0037-0738(99)00133-5), 2000.
- Schwab, K.: Compression and right-lateral strike-slip movement at the Southern Hunsrück Borderfault (Southwest Germany), *Tectonophysics*, 137, 115–126, [https://doi.org/10.1016/0040-1951\(87\)90318-0](https://doi.org/10.1016/0040-1951(87)90318-0), 1987.
- Sintubin, M., Kenis, I., Schroyen, K., Muchez, P., and Burke, E.: “Boudinage” in the High-Ardenne slate belt (Belgium), reconsidered from the perspective of the “interboudin” veins, *J. Geochem. Explor.*, 69–70, 511–516, [https://doi.org/10.1016/S0375-6742\(00\)00034-0](https://doi.org/10.1016/S0375-6742(00)00034-0), 2000.
- Stalder, R., Potrafke, A., Billström, K., Skogby, H., Meinhold, G., Gögele, C., and Berberich, T.: OH defects in quartz as monitor for igneous, metamorphic, and sedimentary processes, *Am. Mineral.*, 102, 1832–1842, <https://doi.org/10.2138/am-2017-6107>, 2017.
- Sterner, S. M., Hall, D. L., and Bodnar, R. J.: Synthetic fluid inclusions. V. Solubility relations in the system NaCl-KCl-H₂O under vapor-saturated conditions, *Geochim. Cosmochim. Ac.*, 52, 989–1005, [https://doi.org/10.1016/0016-7037\(88\)90254-2](https://doi.org/10.1016/0016-7037(88)90254-2), 1988.
- Sumino, H., Dobrzynetskiy, L. F., Burgess, R., and Kagi, H.: Deep-mantle-derived noble gases in metamorphic diamonds from the Kokchetav massif, Kazakhstan, *Earth Planet. Sc. Lett.*, 307, 439–449, 2011.
- Turner, G. and Bannon, M. P.: Argon isotope geochemistry of inclusion fluids from granite-associated mineral veins in southwest and northeast England, *Geochim. Cosmochim. Ac.*, 56, 227–243, 1992.
- Turner, G. and Cadogan, P. H.: Possible effects of ^{39}Ar recoil in ^{40}Ar – ^{39}Ar dating, *Proceedings of the Fifth Lunar Science Conference*, Vol. 2, 5, 1601–1615, <https://ui.adsabs.harvard.edu/abs/1974LPSC....5.1601T/abstract> (last access: 6 August 2024), 1974.
- Turner, G. and Wang, S. S.: Excess argon, crustal fluids and apparent isochrons from crushing K-feldspar, *Earth Planet. Sc. Lett.*, 110, 193–211, 1992.
- Urai, J. L., Spaeth, G., van der Zee, W., and Hilgers, C.: Evolution of mullion (boudin) structures in the Variscan of the Ardennes and Eifel, *Journal of the Virtual Explorer*, 3, 1–16, 2001.
- Van Noten, K., Kenis, I., Hilgers, C., Urai, J. L., Muchez, P., and Sintubin, M.: Early vein generations in the High-Ardenne slate belt (Belgium, Germany): The earliest manifestations of the Variscan orogeny? *Géologie de France*, 2007, 170, <https://lirias.kuleuven.be/1929596> (last access: 6 June 2023), 2007.
- Van Noten, K., Hilgers, C., Urai, J. L., and Sintubin, M.: Late burial to early tectonic quartz veins in the periphery of the High-Ardenne slate belt (Rursee, north Eifel, Germany), *Geol. Belg.*, <https://popups.uliege.be/1374-8505/index.php?id=2485> (last access: 19 January 2019), 2008.

- Van Noten, K., Berwouts, I., Muchez, P., and Sintubin, M.: Evidence of pressure fluctuations recorded in crack-seal veins in low-grade metamorphic siliciclastic metasediments, Late Palaeozoic Rhenohercynian fold-and-thrust belt (Germany), *J. Geochem. Explor.*, 101, 106, <https://doi.org/10.1016/j.gexplo.2008.11.040>, 2009.
- Van Noten, K., Muchez, P., and Sintubin, M.: Stress-state evolution of the brittle upper crust during compressional tectonic inversion as defined by successive quartz vein types (High-Ardenne slate belt, Germany), *J. Geol. Soc.*, 168, 2, <https://doi.org/10.1144/0016-76492010-112>, 2011.
- Villa, I. M.: Direct determination of ^{39}Ar recoil distance, *Geochim. Cosmochim. Ac.*, 61, 689–691, [https://doi.org/10.1016/S0016-7037\(97\)00002-1](https://doi.org/10.1016/S0016-7037(97)00002-1), 1997.
- Virgo, S., Abe, S., and Urai, J. L.: Extension fracture propagation in rocks with veins: Insight into the crack-seal process using Discrete Element Method modeling, *J. Geophys. Res.-Sol. Ea.*, 118, 5236–5251, <https://doi.org/10.1002/2013JB010540>, 2013.
- von Winterfeld, C.-H. : Variszische Deckentektonik und devonische Beckengeometrie der Nordeifel – ein quantitatives Modell, *Aachener Geowiss. Beitr.*, 2, 319, 1994.
- Watson, E. B. and Cherniak, D. J.: Lattice diffusion of Ar in quartz, with constraints on Ar solubility and evidence of nanopores, *Geochim. Cosmochim. Ac.*, 67, 11, [https://doi.org/10.1016/S0016-7037\(02\)01340-6](https://doi.org/10.1016/S0016-7037(02)01340-6), 2003.
- Weil, J. A.: A review of electron spin spectroscopy and its application to the study of paramagnetic defects in crystalline quartz, *Phys. Chem. Miner.*, 10, 149–165, <https://doi.org/10.1007/BF00311472>, 1984.
- Wijbrans, J. R., Pringle, M. S., Koppers, A. A. P., and Scheveers, R.: Argon geochronology of small samples using the Vulkan argon laserprobe, *Proceedings of the Royal Netherlands Academy of Arts and Sciences*, 2, 185–218, 1995.
- Yardley, B. W. D.: Quartz veins and devolatilization during metamorphism, *J. Geol. Soc.*, 140, 657–663, <https://doi.org/10.1144/gsjgs.140.4.0657>, 1983.
- Yardley, B. W. D. and Bottrell, S. H.: Post-metamorphic gold quartz veins from NW Italy – The composition and origin of the ore fluid, *Mineral. Mag.*, 57, 407–422, 1993.
- Ziegler, P. A. and Dèzes, P.: Evolution of the lithosphere in the area of the Rhine Rift System, *Int. J. Earth Sci.*, 94, 594–614, <https://doi.org/10.1007/s00531-005-0474-3>, 2005.